5-2023

Flow Development and Entrainment in Turbulent Particle-Laden Jets

Laura K. Shannon
Washington State University Vancouver

Bianca Viggiano
Portland State University, viggiano@pdx.edu

Raúl Bayoán Cal
Portland State University, rcal@pdx.edu

L. G. Mastin
United States Geological Survey, Cascades Volcano Observatory, Vancouver, WA

Alexa R. Van Eaton
U.S. Geological Survey, Cascades Volcano Observatory

See next page for additional authors

Follow this and additional works at: https://pdxscholar.library.pdx.edu/mengin_fac

Part of the Mechanical Engineering Commons

Let us know how access to this document benefits you.

Citation Details

Authors

Laura K. Shannon, Bianca Viggiano, Raúl Bayoán Cal, L. G. Mastin, Alexa R. Van Eaton, and Stephen Solovitz

JGR Atmospheres

RESEARCH ARTICLE

Key Points:

- Experiments study an analogue, particle-laden volcanic jet over a range of Reynolds numbers, Stokes numbers, and particle mass loadings
- Particle image velocimetry determines local flow velocities, entrainment, and turbulent flow statistics in the jet and the ambient
- High-inertia particles subdue entrainment and turbulent fluctuations for a cylindrical vent, which can reduce the collapse criterion by 3X

Correspondence to:
S. A. Solovitz,
stevesol@wsu.edu

Flow Development and Entrainment in Turbulent Particle-Laden Jets

Laura K. Shannon[1], Bianca Viggiano[2], Raúl B. Cal[2], Larry G. Mastin[3], Alexa R. Van Eaton[3], and Stephen A. Solovitz[1]

[1]School of Engineering and Computer Science, Washington State University Vancouver, Vancouver, WA, USA, [2]Department of Mechanical & Materials Engineering, Portland State University, Portland, OR, USA, [3]U. S. Geological Survey, Cascades Volcano Observatory, Vancouver, WA, USA

Abstract Explosive eruptions expel volcanic gases and particles at high pressures and velocities. Within this multiphase fluid, small ash particles affect the flow dynamics, impacting mixing, entrainment, turbulence, and aggregation. To examine the role of turbulent particle behavior, we conducted an analogue experiment using a particle-laden jet. We used compressed air as the carrier fluid, considering turbulent conditions at Reynolds numbers from approximately 5,000 to 20,000. Two different particles were examined: 14-µm diameter solid nickel spheres and 13-µm diameter hollow glass spheres. These resulted in Stokes numbers between 1 and 35 based on the convective scale. The particle mass percentage in the mixture is varied from 0.3% to more than 20%. Based on a 1-D volcanic plume model, these Stokes numbers and mass loadings corresponded to millimeter-scale particle diameters at heights of 4–8 km above the vent during large, sustained eruptions. Through particle image velocimetry, we measured the mean flow behavior and the turbulence statistics in the near-exit region, primarily focusing on the dispersed phase. We show that the flow behavior is dominated by the particle inertia, with high Stokes numbers reducing the entrainment by more than 40%. When applied to volcanic plumes, these results suggest that high-density particles can greatly increase the probability of column collapse.

Plain Language Summary Volcanic eruptions eject a mixture of gases and solid particles at high speed. The particles affect the flow behavior, which may impact the growth of a plume and its mixing with the atmosphere. To study this phenomenon, we conducted a laboratory-scale experiment using an air jet containing small particles. We varied the jet speed, the particle type, and the particle density, and we measured the local flow velocities within the jet and the surrounding air. The particle inertia significantly influenced the behavior, as denser particles dampened flow mixing and turbulence. This reduced the inflow of air to the jet, which is important to the growth of a volcanic plume. The presence of large particles can increase the likelihood that the plume would collapse.

1. Introduction

Volcanic eruptions can eject large quantities of ash particles into the atmosphere, posing hazards to health, infrastructure, and air travel (Wilson et al., 2015). In the event of an eruption, rapid forecasts of ash transport are needed to guide both local and distant populations, as sub-millimeter-diameter particles can potentially travel hundreds to thousands of kilometers (Stevenson et al., 2015). Accurate modeling requires an understanding of the flow behavior, which is challenging to forecast due to the turbulent, multiphase conditions. In particular, volcanic particles modify the development of an ash plume, affecting entrainment, mixing, and eventually ash fallout.

Entrainment plays an important role in the growth of a volcanic plume (Costa et al., 2016). In an eruption, the expelled mixture is typically denser than the surrounding air, so it is negatively buoyant. As the jet rises, air is entrained from the ambient environment and heated by the warmer volcanic particles, which can reduce the overall density and result in positive buoyancy. Depending on the amount of entrainment, this transition to buoyant conditions may be delayed or even prevented, leading to collapse of the column (Solovitz & Mastin, 2009). Even without collapse, the entrained air dilutes the mixture, changing the plume density and its overall vertical distribution of mass in the atmosphere. Many plume models incorporate entrainment through empirical parameters, which are determined through field observations and analogue experiments (Agrawal & Prasad, 2003; Briggs, 1965; Fischer et al., 1979; Morton et al., 1956; Suzuki & Koyaguchi, 2015). Recent studies demonstrate

Writing – review & editing: Raúl B. Cal, Alexa R. Van Eaton, Stephen A. Solovitz

that particles modify entrainment, particularly in the buoyant region (Cerminara et al., 2016; Gilchrist & Jellinek, 2021; Jessop & Jellinek, 2014; Lherm & Jellinek, 2019). However, there is more uncertainty in the developing, near-exit region.

More locally, the mixing process is driven by turbulent eddies within the flow, which also impact the preferential concentration of particles within the multiphase flow (Pumir & Wilkinson, 2016). Small-scale eddies promote the collision rate of particles (Sundaram & Collins, 1997), which collect into specific regions within the turbulent flow (Coleman & Vassilicos, 2009; Eaton & Fessler, 1994; Squires & Eaton, 1990; Sumbekova et al., 2017). In many eruptions, ash particles can then aggregate together and fall out relatively close to their source. However, the particles themselves modify the turbulence, either augmenting or attenuating velocity fluctuations at different conditions (Balachandar & Eaton, 2010). While mechanisms have been identified for this turbulent behavior, their relative influence is not well quantified.

Most particle-laden studies consider fundamental flows such as homogeneous turbulence, often at relatively low Reynolds numbers. However, the geometry can have a significant influence on preferential concentration, with greater clustering within saddle regions of a shear layer (Longmire & Eaton, 1992; Squires & Eaton, 1990). In the near-exit region of an eruption, the flow exhausts like a jet, driven primarily by momentum. Particle-laden jets have been examined since the 1960s, originally focusing mostly on the gas phase (Balachandar & Eaton, 2010). By the 1990s, more advanced techniques permitted separate examination of the particle and gas phases. However, as noted by Lau and Nathan (2014), these studies considered only high-inertia particles, polydisperse distributions, and point measures such as laser Doppler anemometry (LDA) and phase Doppler anemometry (PDA). For example, Prevost et al. (1996) used PDA to study the behavior of a vertically downward air jet laden with glass particles of different sizes. Larger particles displayed significant inertial effects, with the jet profile developing more slowly than a single-phase jet. Longmire and Eaton (1992) applied LDA to examine a periodically forced air jet containing glass particles, which permitted both mean and phase-averaged analysis. Particles again lagged the fluid speeds seen in unladen conditions, though the turbulent fluctuations remained significant farther downstream. The peak fluctuations occurred in regions of high strain, aligned with locations where particles clustered. These clusters persisted even for very high mass loadings of particles.

While point measures can provide valuable information about the turbulent flow behavior, they are unable to assess the full instantaneous flow field. Particle image velocimetry (PIV) provides an alternate solution, using cross-correlation of full field images to ascertain local velocity distributions. For isotropic, particle-laden flow, PIV has been used to demonstrate attenuation of turbulence (Hwang & Eaton, 2006), sub-Kolmogorov scale variation (Tanaka & Eaton, 2010), and particle collision behavior (Hoffman et al., 2020). Sakakibara et al. (1996) conducted perhaps the first PIV study of particle-laden jets, examining both the fluid and particle motion to determine turbulent modeling parameters. This study considered a periodically forced jet, similar to Longmire and Eaton (1992), and the particle mass loading was very dilute. As a result, only a few particles were visible in each image, but they were sufficient to estimate turbulent dissipation. More recently, Lau and Nathan (2014, 2015, 2017) have undertaken an extensive study of particle-laden jets emanating from a long circular pipe. Using a vertically down air jet with a weak coflow, they considered the response for a range of glass particle sizes at a high mass loading, including low-inertia cases where the particles followed the flow more faithfully. Through measurements of the mean velocities and concentrations, they observed slower flow development when the particle inertia was high (Lau & Nathan, 2014). In addition, these particles were initially concentrated near the walls at the exit, which was attributed to the flow conditions exiting the pipe. Later study demonstrated that particle clusters were generated within the vertical pipe, likely due to coherent wall structures within that turbulent flow (Lau and Nathan, 2015, 2017).

Although this flow has been examined for several decades, there are still significant issues. There is fairly limited data at flow conditions pertinent to volcanic plumes, particularly when considering variation in mass loading and inertial response. For example, the most relevant previous study considered a single mass loading of 40% (Lau & Nathan, 2014), while volcanic eruptions generate a wide range of particle loadings. In addition, more research is needed to understand entrainment in particle-laden jets, which is important for plume ascent (Solovitz & Mastin, 2009). Until more recently, most experiments used point measurements, which do not permit examination of the instantaneous influence of particle fluctuations on their neighbors. More subtly, the initial and boundary conditions differ between the various experiments, which can influence the preferential concentration of particles immediately after flow ejection. To address the issues outlined above, we have conducted a suite of
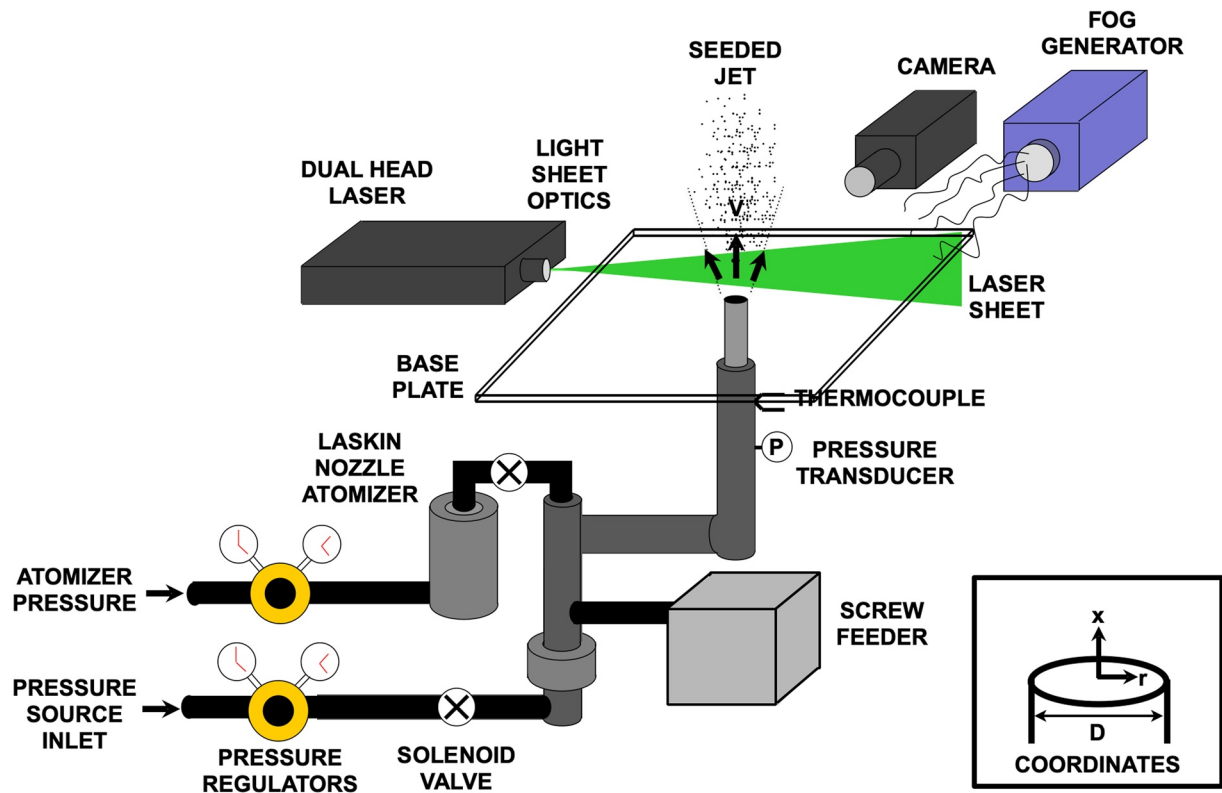
Figure 1. Schematic of experimental jet apparatus, adapted from Solovitz et al. (2011). The inset shows the coordinate axes. The exit diameter, D, is 6.83 mm.

PIV experiments on particle-laden jets. Using a well-characterized vertically upward air jet, we vary the flow exit velocity, particle density, and particle feed rate over a range of conditions pertinent to volcanic eruptions. We measure the mean and turbulent velocity fluctuations of the particles, which reveal entrainment behavior, particularly with high-inertia particles.

2. Experimental Methods

2.1. Jet Apparatus

We used a rigid pipe apparatus, displayed schematically in Figure 1, to generate a vertical jet within a large laboratory at Washington State University Vancouver. This system is adapted from a structure originally developed by Solovitz et al. (2011), which has been described in detail previously. At its inlet, depicted at the lower left, laboratory compressed air was fed into the system, where it was regulated to a constant pressure level. This primary flow passed through a series of rigid pipes before turning vertically upward into a constant-diameter pipe. The flow diameter then contracted from 15.8 to 6.83 mm using a tapered nozzle following a fifth-order polynomial, which ensured uniform flow (Bell & Mehta, 1988). Downstream of the nozzle, the pipe diameter remained constant over approximately 15.2 cm before ejecting into the laboratory. The nondimensional length of this final pipe was sufficient for fully developed turbulent conditions at the exit (Kays & Crawford, 1993) for typical test speeds (~10 to 50 m/s). Previous measurements of the exit velocity profile in air matched the expected logarithmic dependence seen when fully developed (Saffaraval & Solovitz, 2012). The pipe exit was placed at the center of a rigid, horizontal plate with length and width of 61 cm each. The edges of the plate were approximately 45 jet diameters from the centerline.

The flow was monitored near the exit using a gage pressure transducer and a T-type thermocouple, each placed just ahead of the nozzle. An additional pressure transducer was located at the regulator near the system inlet. In all cases, these sensors were used to help verify that the flow conditions remained steady throughout the experiment. The actual exit conditions were measured directly through PIV, as described later, but this analysis required post-processing of the flow velocities.

The entire apparatus was placed within a large enclosure with flexible plastic walls, which served to isolate the system from the rest of the laboratory. This reduced the impact of flow variation in the facility, as well as protecting electronics from ejected particles. The enclosure was 2.44 m wide, 2.44 m long, and 3.66 m tall, and the jet exit was positioned along its vertical centerline. At this location, the sidewalls were approximately 180 diameters from the jet. The enclosure was designed so that flow recirculation would not be significant, with the jet momentum changing by less than 1% (Hussein et al., 1994).

2.2. Flow Seeding

Particles were supplied from a commercial screw feeder, which provided a constant mass flow rate for up to thirty minutes of testing. This device featured a simple adjustment knob for output control, which could control the feed rate to within ±2% resolution. The head of the feeder was fitted into a large-diameter section of the apparatus, and it was held in place using a compression fitting. The particle hopper was also bolted closed using a rigid metal plate, which helped equilibrate pressures within the feeder and the jet fixture. The feeder screw propelled a calibrated quantity of particles through an opening into the apparatus, which was oriented downward so that gravity aided their fall into the apparatus. The large-diameter region served as a fluidized bed, which was generated by passing the system compressed air upward through a porous disc at its base. This chamber produced a dilute, mixed flow of particles within the fluidized bed. The fluidized mixture exited through a smaller diameter passage, which used a Venturi effect to help pull the particles into the flow. This mixture then traveled through the remainder of the system to the apparatus exit.

Two types of particles were studied: 14-μm solid nickel spheres and 13-μm hollow glass spheres. Although these particles had nearly the same diameter, their densities were significantly different. The nickel density was 8,900 kg/m^3, while the effective density of the hollow glass was only 1,100 kg/m^3, resulting in different inertial behavior. The particle size was verified using a laser diffraction particle size analyzer at the US Geological Survey Cascades Volcano Observatory. For the nickel, the mean diameter was 13.9 μm with a standard deviation of 1.8 μm, and more than 80% of particles (by volume) were between 9 and 17 μm. For the hollow glass, the mean diameter was 13.2 μm with a standard deviation of 1.6 μm, and 80% of the diameters were between 7 and 25 μm. The majority of the hollow glass spheres outside this range were smaller, and they had a negligible influence on the flow.

Prior to installation, the screw feeder was calibrated for each type of test particle. After filling the feeder hopper, the unit was operated at a specific control setting, which ejected particles from the head opening. The device ran for two minutes, and the output was weighed using a 8.2-kg scale with a resolution of ±1 g. The measurements were performed at four different control settings over its full range, and these tests were each repeated twice. For each particle type, the feeder flow rate was linear with a squared correlation coefficient $R^2 > 0.99$. Based on the scale resolution and the calibration, the uncertainty in feed rate was estimated at ±2%. A similar calibration was also performed after installation within the apparatus, which showed deviations smaller than the system resolution.

During operation, most particles traveled through the apparatus and out of the jet exit. However, a finite quantity remained within the fluidized bed and the system piping. To account for this mass, the particle feeder and the fluidized bed were both weighed before and after each experiment. The pipe apparatus was vacuumed thoroughly to capture any remaining particles, and the vacuum bag was also weighed before and afterward. After subtracting the mass remaining within the fluidized bed and the apparatus, the actual particle mass was determined. This quantity was used to determine the mass loading of the experiment. In a typical experiment using nickel particles, more than 75% of the particles originally injected by the screw feeder traveled out into the jet flow. The PIV images were also examined over time, and these showed a consistent particle output rate.

Besides these primary particles, the flow could also be seeded using a Laskin nozzle atomizer. Using a second, regulated compressed air source, this device generated 1-μm diameter olive oil droplets, which were injected into the apparatus well upstream of the exit. At the flow conditions considered, these droplets were small enough to faithfully follow the air velocity fluctuations without significant inertial effects (Melling, 1997). In most experiments, either the screw feeder or the atomizer was used independently, as the combination would coat the inside of the apparatus with a mixture of these seeding materials. The atomizer was primarily used to study a baseline, unladen flow condition. Because the screw feeder and atomizer only seeded the jet itself, the rest of the
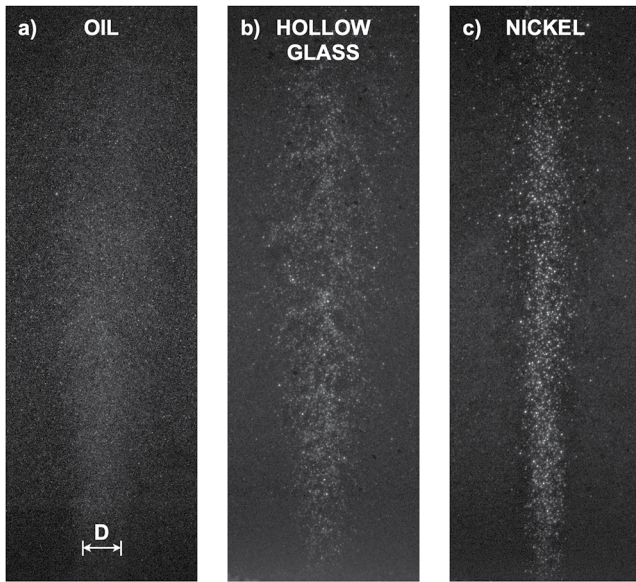
Figure 2. Sample images near the jet centerline for (a) single-phase air only (with oil droplets), (b) hollow glass-laden air, and (c) nickel-laden air. These display a region of interest with a width of 508 pixels (5.0 exit diameters) and a height of 1,524 pixels (15.0 exit diameters) for the raw camera images. The scale bar shows the size of one exit diameter, D.

test chamber was filled with a dilute dispersion of aqueous glycol droplets from a commercial fog generator. At operating conditions, the glycol drops were typically 1 μm in diameter, which also followed the air flow faithfully within the facility (Melling, 1997). This fog was used to examine entrainment into the jet flow, as well as to observe any recirculation within the chamber.

2.3. PIV System

We used a commercial PIV system to examine the flow behavior near the jet exit. A dual-head, frequency-doubled Nd:YAG laser produced two successive 50 mJ pulses of 532-nm wavelength light. Each pulse had a duration of 5 ns. The beams passed through a diverging cylindrical lens and a converging spherical lens, which converted each pulse into a light sheet that passed through the jet centerline. At the jet exit, the light sheet was approximately 0.5 mm thick, and it illuminated a rectangular region approximately 8.5 cm tall and 17 cm wide. In the axial flow direction, we could observe more than 12 jet diameters downstream. This light scattered off of the seed particles and oil tracers passing through the flow region.

A 4-megapixel charge-coupled device (CCD) camera was aligned perpendicular to the light sheet, with the image focused on the illuminated particles within the sheet. The camera and the laser were both operated using a synchronizer unit, which triggered each simultaneously. The two laser pulses were delayed by a fixed time duration, during which the particles traveled within the sheet. This time delay was varied for each specific test condition, but it was typically on the order of 20 μs when examining the jet centerline. By examining the motion of these tracers between the two camera images, we could determine the local velocity field.

Figure 2 displays sample particle images near the jet centerline for three typical test cases: single-phase air only, hollow glass-laden air, and nickel-laden air. With air alone, the flow near the centerline was seeded with olive oil tracers. For the two particle-laden air cases, the particles themselves were used for seeding, with no additional olive oil added. In all three cases, the region outside of the jet centerline was seeded with aqueous glycol droplets, which were generally smaller and dimmer. The different particle types could clearly be distinguished due to their size and relative brightness. Near the exit, the particle density did not vary significantly across the profile, indicating a uniform particle distribution. There was some clustering downstream, notably with the hollow glass particles. We discuss the particle behavior in more detail when examining the test conditions in Section 2.4 later.

It is critical to note that the particle-laden measurements focused on the particle velocities, not the carrier fluid. Without the olive oil tracers, we were not observing the motion of the air around the particles. This is particularly important when examining turbulent velocity fluctuations, as high inertia particles would not respond in the same manner as the air. In some previous experiments, separate measurements considered the individual fluctuations for the particles and the air (Sakakibara et al., 1996). In this experiment, we were primarily concerned with the particle velocity behavior, which would relate to the interaction between solid ash particles in an eruption. Even so, we did consider a single-phase air case as a baseline for comparison.

The image pairs were analyzed using Pivlab2000 (Han, 2001), which divided each image into smaller interrogation regions. The sub-regions were cross-correlated, providing the average particle displacement within that region. We applied a Gaussian fit for the cross-correlation peak, which resulted in sub-pixel accuracy for the displacement without significant peak locking. For each image, the algorithm used multiple passes with successively smaller regions to improve the resolution. Each cross-correlation used the average displacement from the previous iteration as an initial estimate, improving the signal-to-noise ratio for the correlation. For these experiments, the initial interrogation region size was 128 pixels by 128 pixels, while the final size was 32 pixels by 32 pixels. The smallest region size was chosen to maintain sufficient particles for accurate displacement estimates, which was typically six at a minimum (Raffel et al., 1998). During the processing, a 50% overlap was applied between interrogation regions, which resulted in a vector spacing of 1.1 mm in each direction. The region size

was also used to determine the appropriate time delay between images. For minimum processor uncertainty, the largest particle displacement was less than one-quarter of the smallest interrogation region size, or 8 pixels. These displacements were converted to physical dimensions using a calibration factor of 67.16 μm/pixel, which was measured using a custom calibration target placed within the image plane. The target consisted of a uniform grid of 6.35 by 6.35 mm square posts extending across the entire image, so the calibration factor considered both the axial and transverse directions.

Following each iteration, the instantaneous fields were filtered to remove errant vectors. First, a range filter eliminated any displacements that exceeded realistic magnitudes. Since the maximum particle displacement was less than 8 pixels, we filtered any vectors that exceeded this level by more than 25%. Second, we applied a consistency filter, which examined the similarity of a local vector to its eight adjacent neighbors. If the local displacement differed from half of these neighbors by more than 5 pixels, it was eliminated. For subsequent iterations, any filtered vectors were replaced with an interpolated value from the eight neighbors. The resulting vector fields found accurate vectors for more than 95% of the interrogation regions, with more than 85% converging without interpolation. The velocity uncertainty was determined through a propagation-of-uncertainties technique. Based on the interrogation sizes and the cross-correlation algorithm, the typical processor accuracy was ±0.1 pixels (Raffel et al., 1998). When compared to the peak displacement, this corresponded to an uncertainty of approximately ±1.3%. In addition, we included the uncertainties due to the synchronizer timing and the camera calibration factor, though these had nearly negligible influence compared to the processor. During our later analysis, we used additional flow metrics, such as the entrainment ratio and the turbulent velocity variance. The entrainment ratio was calculated using the quotient of a radial velocity with the centerline velocity, which was evaluated through a linear regression. When incorporating the uncertainty due to that regression method (Solovitz & Mastin, 2009), the entrainment ratio had an overall uncertainty of ±5.9%. The variance was determined using the instantaneous velocity fluctuations relative to the ensemble-averaged velocities, so we included the individual uncertainties for each velocity term. Along the centerline, the overall uncertainty in the peak variance was estimated at ±14%.

2.4. Experimental Test Parameters

We varied three conditions to study the particle laden-flow behavior, specifically the jet exit velocity, the particle density, and the particle feed rate (as shown in Table 1). We examined three different exit velocities for two different particle types. For the higher velocities, we also considered three different particle feed rates. At all three velocities, we acquired data using olive oil tracers alone, which serve as the baseline case with 0% loading. The test cases were selected to examine a wide range of nondimensional conditions, specifically examining the Reynolds number (Re_D), the Stokes number (St), and particle mass loading (Φ).

The Reynolds number relates inertial forces in the fluid to the viscous forces, and it is defined as $Re_D = \rho V D/\mu$. Here, ρ is the fluid density, V is the jet exit velocity, D is the jet exit diameter, and μ is the viscosity of the air carrier fluid. We considered a range where Re_D varied from approximately 5,000 to 20,000, which is well within the fully turbulent range. In addition, the flow within the pipe should also be fully turbulent for these conditions. In actual eruptions, the Reynolds number can extend over a very large range, from $\sim 10^3$ to $> 10^9$ (Sparks et al., 1997). Hence, we studied conditions in the lower portion of this range.

The Stokes number is a ratio of time scales, which is the inertial response time of the particles divided by the fluid response time. If we use the convective time scale as the fluid response time, this number is defined as $St = \rho_p D_p^2 V/(18\mu D)$. Here, ρ_p is the particle density, and D_p is the mean particle diameter. Note that the convective scale, D/V, has similar scaling to the turnover time for the large-scale jet eddies. We examined a range of Stokes numbers from near 1 to more than 35. Typically, particles have significant inertial effects for St >> 1, while they faithfully follow the fluid when St << 1. If St ~ 1, the particle and fluid responses are comparable. Our experiments extended from this regime to conditions when inertia should dominate. Still, even at St ~ 35, the fluid behavior can impact preferential concentration of particles (Banko, 2018). Eruptions can have Stokes numbers extending from <<1 to >>1, depending on which portion of the plume is considered. Near the exit, where flow speeds are high, we expect St > 1.

Note that there are other definitions of the Stokes number. One uses a turbulent, Kolmogorov time scale rather than the convective scale (Hwang & Eaton, 2006), which leads to much higher values. This time scale, $\tau_k = (\nu/\varepsilon)^{1/2}$, is dependent on the fluid kinematic viscosity, ν, and the dissipation rate, ε. For a fully developed jet, the dissipation is estimated from the correlation $\varepsilon \approx 0.034\ V^3/D$, which is based on dimensional scaling and classic experiments

Table 1
Experimental Test Conditions for Different Particles

Particle type	Exit velocity V (m/s)	Reynolds number $Re_D = \rho V D/\mu$	Stokes number $St = \rho_p D_p^2 V/(18\mu D)$	Mass loading $\Phi = \dot{m}_p / \dot{m}_f$
Nickel (14 μm)	11.4	4940	9.0	3.6%
				9.7%
				14.4%
	22.1	9600	17.4	3.9%
				14.6%
				18.9%
	44.3	19300	34.9	6.4%
				14.0%
				21.4%
Hollow glass (13 μm)	11.4	4940	1.0	0.3%
				1.5%
				3.0%
	22.1	9600	1.9	0.3%
				1.3%
				2.0%
	44.3	19300	3.7	0.5%
				1.2%
				1.21%

(Pope, 2000). Using this time scale, our test conditions correspond to Stokes numbers from 13 to more than 800. Dissipation rates do differ in the developing, near-exit region, but the order of magnitude is similar. The Kolmogorov scale represents the smallest eddies within the flow, which have a size, $(\nu^3/\varepsilon)^{1/4}$, smaller than 27 μm in all of our test cases. Because this is below our PIV resolution of 1.1 mm, this scale cannot be measured directly. The turbulence extends over a wide range of sizes, and most energy is concentrated in the largest eddies. Hence, another Stokes number definition uses an eddy turnover time, which is a ratio of the eddy diameter with its rotation speed. For a jet, the largest eddies have a size comparable to the jet diameter, D. Their rotation speed is related to the turbulent fluctuation speed, which in on the order of 0.25 V (Pope, 2000). The resulting turnover time is directly proportional to the convective time scale, D/V, though it is larger by a scalar factor greater than one. For our test conditions, the range of Stokes numbers is between 0.3 and 10 using the turnover time. Yet another Stokes number definition includes a correction to the particle time scale (Balachandar & Eaton, 2010), which divides the characteristic time by $f = 1 + 0.15Re_p^{0.687}$. Here, Re_p is a particle Reynolds number, which is based on the particle diameter and velocity relative to the surrounding fluid. Assuming that the relative velocity is comparable to the turbulent fluctuation speed, this correction factor ranges from 1 to 1.7 in our experiments, resulting in Stokes numbers from 0.8 to 20. For consistency with earlier particle-laden jet studies (Lau & Nathan, 2014) and the link to the turnover time, we used the Stokes number based on the standard convective scale.

The mass loading is a ratio of mass flow rates, $\Phi = \dot{m}_p / \dot{m}_f$, comparing the particle flow rate to the fluid flow rate. We studied cases from 0.3% to 21.4%, ranging from dilute conditions to heavily laden flows. Eruptions often contain significant particle loading, exceeding more than 90% at the exit, while reaching 5%–10% at 2–4 km of elevation (Mastin, 2007). We covered an appropriate range for the lower to middle portions of the jet. In the experiments, the nickel particles had a higher mass loading due to their density, as the screw feeder was limited in its volumetric output. Even so, several test cases overlapped with $\Phi \sim 3\%$, which permitted comparison of the response at different Re_D and St. We also studied an unladen, 0% case to provide a baseline for single-phase air flow only. Technically, these oil droplets (and those in the ambient) are a second phase embedded within the air carrier fluid. However, the oil is very dilute, with a volumetric loading near 10^{-8} and a mass loading on the order of 10^{-5}. In addition, the Stokes numbers for these droplets are less than 0.02 based on the convective scale, so they move with the carrier fluid without significant deviation (Melling, 1997).

In these experiments, we do not specifically focus on buoyancy effects, which are relatively small within the particle-laden air jet. Buoyancy is often characterized by the Richardson number, $Ri = \Delta\rho gD/(\rho V^2)$, which represents a ratio of buoyant forces to inertial forces. Here, $\Delta\rho$ is the density difference between the jet and the ambient, and g is the gravitational acceleration. Even for our highest mass loadings, $Ri < 10^{-4}$, and most cases have $Ri < 10^{-5}$. Hence, the buoyant effects should be very small in the test region. This conclusion is also supported by another metric, the sedimentation number, Σ. This parameter equals the ratio between the particle settling velocity, $\rho_p D_p^2 g/(18f\mu)$, and the jet speed, V (Carazzo & Jellinek, 2012). For our experiments, $\Sigma < 0.004$ at the highest loadings, and $\Sigma < 0.001$ in most tests. This further indicates that the gravitational settling effects are much smaller than the inertial effects.

For each experiment, we acquired a total of 2,000 image pairs using the PIV system. Of these, 1,000 used short time delays between images, which allowed study of the highest speed flows near the jet centerline. Typically, the delay was near 20 µs. The remaining 1,000 used longer time delays to examine the entrained flow in the ambient region around the jet. The entrained velocities are much lower than the centerline speed, with magnitudes on the order of 2% of the exit velocity at a radial position of one diameter. At the original time delay, the imaged particles are displaced less than 0.2 pixels in this ambient region, which is only slightly above the PIV processor accuracy. To improve the resolution, we increased the time delay between the images, resulting in particle displacements well above the processor accuracy. For these cases, the delay was typically 200 µs. We could also use the first set of 1,000 image pairs to examine the entrainment, but the velocity resolution was coarser. The number of image pairs was selected to permit reasonable accuracy for both mean and turbulent velocity statistics while maintaining a sufficient particle flow throughout. Previous experiments (Saffaraval & Solovitz, 2012) demonstrate good convergence when using more than 500 image pairs, and we were beyond this total.

3. Results

3.1. Flow Fields

At each test condition, we examined the velocity flow fields to study the jet behavior. Figure 3 shows sample instantaneous vector fields for three cases, which consider single-phase flow with air only, particle-laden flow with hollow glass spheres, and particle-laden flow with solid nickel spheres, respectively. All three have the same Reynolds number of 9,600, and the two particle-laden cases have similar mass loadings near 3%. The primary difference is the Stokes number, which ranges from near zero to more than 17. The vector fields are overlaid by instantaneous vorticity contours, $\omega = \partial v_z/\partial x - \partial v_x/\partial z$, which are normalized by the exit velocity, V, and the exit diameter, D. The velocity components, v_x and v_z, are the axial and transverse velocities, respectively. Similarly, the coordinates, x and z, are the axial and transverse positions. Each of these is normalized by the exit diameter. (To match the vorticity in cylindrical coordinates, we invert the sign of the vorticity for $z < 0$.)

There are clear similarities between the first two fields, which display single-phase air and hollow glass-laden air, respectively. In both cases, velocity fluctuations are significant within the jet core, even very close to the exit. The vorticity is strongest in the shear layer along the jet boundary, which is initially located at transverse positions, z, of $\pm0.5D$ from the centerline. However, there is some instantaneous variation near the centerline in both fields. The third field is distinctly different. In this nickel-laden flow, there are few velocity fluctuations within the jet core over the entire imaged window. The high-vorticity shear layer remains vertical well downstream, and it does not approach the centerline. This layer is located slightly farther out from the centerline, with peak vorticity at transverse positions of $z \approx \pm0.7D$ from the centerline. Outside of the jet core, all three fields show some fluctuations in the ambient region.

We then ensemble-averaged all of the instantaneous velocity fields for each test condition to examine the mean flow structure. Figure 4 displays the mean velocity vector fields for the same three cases from Figure 3. Again, these are overlaid with the mean vorticity contours, which are symmetric for each jet. The averaged fields are much smoother than their instantaneous counterparts, which partly masks the differences in the three flow fields. Even so, the nickel-laden jet features a wider jet core, with the shear layer vorticity concentrated at a larger radial distance. For a more rigorous comparison, though, we must consider the specific velocity profiles and instantaneous statistics.

3.2. Mean Flow Structure

Next, we used the ensemble-averaged velocities to examine the mean flow structure for different conditions. Because the three nondimensional parameters had some overlap, as seen in Table 1, we could isolate the effects
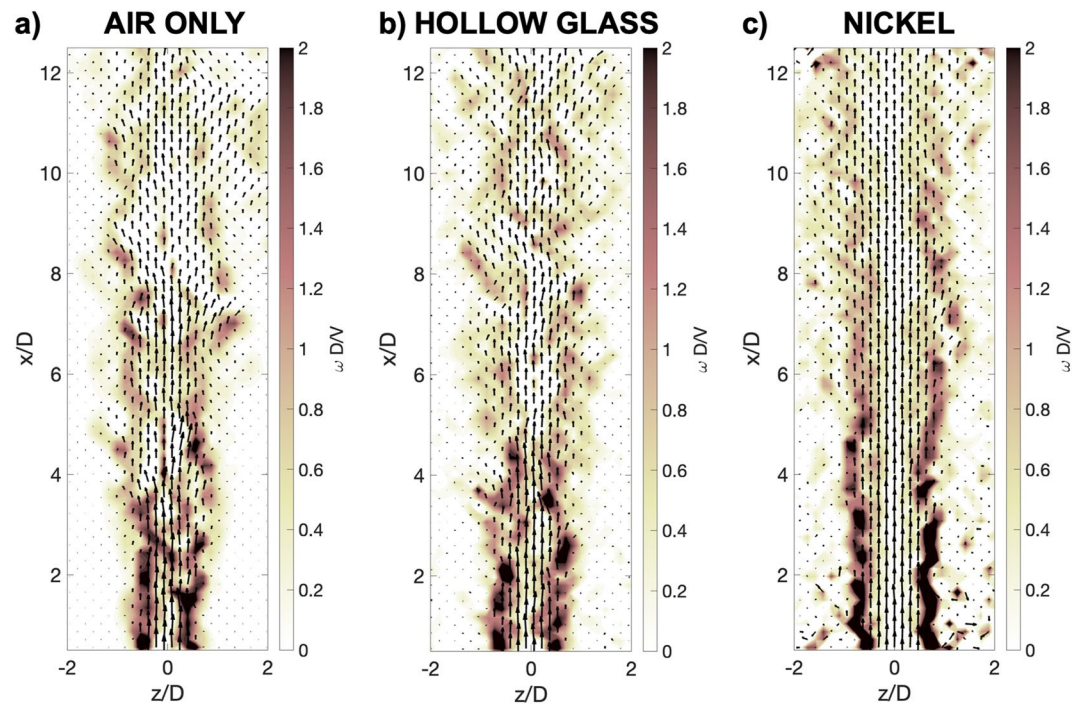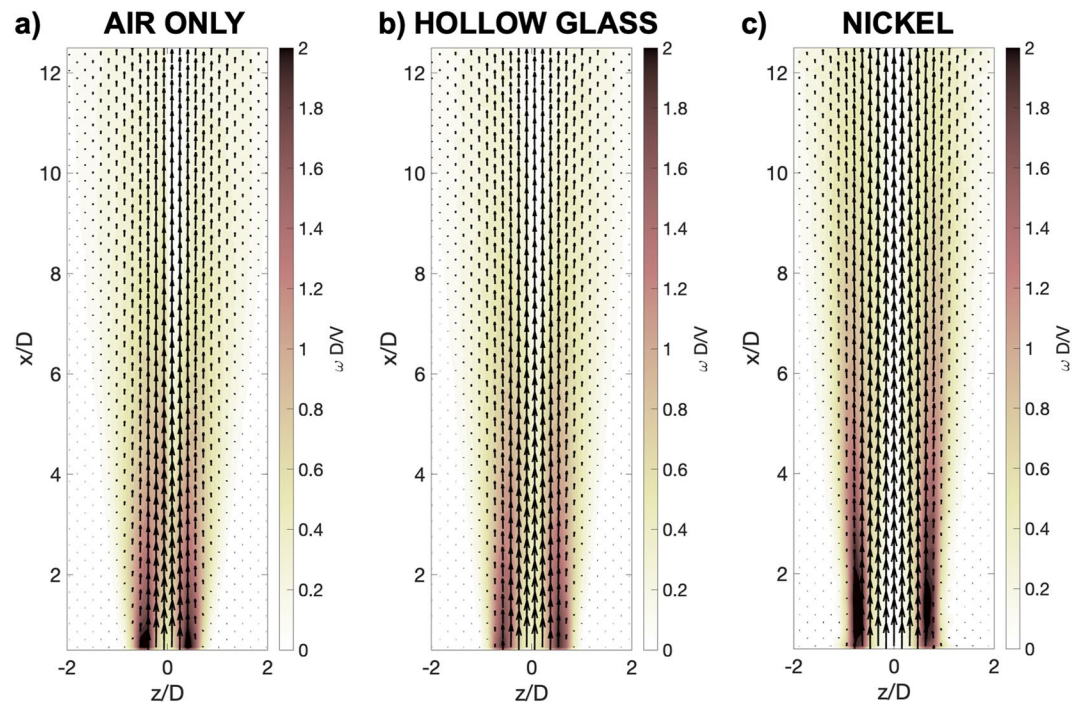
Figure 3. Sample instantaneous velocity vector fields near the jet centerline for (a) single-phase air only, (b) hollow glass-laden air (St = 1.9), and (c) nickel-laden air (St = 17.4). Each case has the same Reynolds number of 9,600, and the particle-laden cases have mass loadings near 3%. The vector density is reduced by 50% in each direction for visual clarity. The fields are overlaid by instantaneous vorticity contours. The position and velocity components are normalized by the exit diameter and velocity, respectively.

of each one individually. First, we observed the effect of the Reynolds number, which should have a secondary influence when in the turbulent flow regime. Figure 5a displays the ensemble-averaged axial velocity along the jet centerline, U_c, at three different exit speeds. These correspond to Re_D from approximately 5,000 to 20,000. The velocity is normalized by the centerline speed at the exit, while axial position is normalized by the jet diameter. All three cases considered air laden with nickel particles with a mass loading of $\Phi \sim 14\%$. Note that the Stokes number also depended on the exit speed, so its value was not the same for the three cases, ranging from 9.0 to 34.9. Still, each has St >> 1. To be clear, we measured the velocities of the particles—not the air carrier fluid. In this two-phase flow, each phase may have different behavior. For an application, the particle velocity is critical, as the relative motion would affect local clustering.

The centerline speed showed some dependence on the Reynolds number, as the particle exit speed persisted farther downstream at higher values. For $Re_D = 4,940$, the centerline speed began to decrease at $x/D \sim 2$, indicating a smaller potential core. At $Re_D = 19,300$, the speed did not change significantly until $x/D \sim 8$. This was an initial indication of the importance of inertia, as higher-speed jets maintained their exit conditions longer. However, because these three cases had differing Stokes numbers, we cannot conclude that this behavior was solely due to Reynolds number.

Second, we independently considered the effects of the Stokes number, which should be the most important factor for particle clustering. Figure 5b displays the centerline velocity for jets laden with different particles. In each case, the Reynolds number was fixed at $Re_D = 9,600$. Two particle-laden flows are shown, each with a mass loading $\Phi \sim 3\%$. One featured nickel, whose particles had high inertia at St = 17.4. The other used hollow glass, which was more responsive to flow fluctuations due to its lower St = 1.9. For the particle-laden cases, we show the velocity of the particle phase, which differs from a single-phase fluid. To demonstrate this effect, we also included a baseline, unladen case at $\Phi = 0$ for comparison. This baseline agrees well with previous experimental data for a single-phase jet (Mi et al., 2007), particularly after x/D = 6. That earlier experiment considered a higher Reynolds number of 72,000, so it maintained slightly higher speeds near the exit. The behavior was distinctly different at higher Stokes numbers. With hollow glass spheres at lower St, the particle velocity profile closely

Figure 4. Ensemble-averaged velocity vector fields near the jet centerline for (a) single-phase air only, (b) hollow glass-laden air (St = 1.9), and (c) nickel-laden air (St = 17.4). Each case has the same Reynolds number of 9,600, and the particle-laden cases have mass loadings near 3%. The vector density is reduced by 50% in each direction for visual clarity. The fields are overlaid by mean vorticity contours. The position and velocity components are normalized by the exit diameter and velocity, respectively.

resembled that of the air alone, falling off significantly downstream. From the exit to x/D = 12, the axial velocity decreased to approximately 45% of the exit condition in both cases. The hollow glass had slightly higher centerline speeds from x/D ∼ 2 to 8, but this deviation was negligible beyond. However, the high-St nickel particles showed almost no change in centerline speed over the first portion of the test range. At x/D = 6, the centerline speed was only 5% less than the exit value, while the hollow glass-laden jet speed was almost 25% lower. With the nickel particles, there was even a slight rise until x/D ≈ 4, showing that the particles were still accelerating beyond the exit. Afterward, the nickel particles slowed far more gradually than the air and hollow glass, remaining at 70% of the exit speed at x/D = 12. This weak acceleration and deceleration agreed with the LDA measurements from Longmire and Eaton (1992). This behavior was due to the difference between the particle and gas phase speeds at the exit, as the gas traveled slightly faster than the high-inertia particles.

Third, we examined the influence of mass loading. Figure 5c shows the centerline axial velocities with different mass loadings, using the same normalizations. Three mass loadings of nickel particles were considered, ranging from 3.9% up to 18.9%. The Reynolds number, Re_D, was 9,600, while the Stokes number, St, was 17.4. For all three particle-laden cases, the particle centerline velocity behaved nearly identically, deviating by less than 2% from each other. Each maintained the same speed until x/D ∼ 6, after which there was a gradual drop to approximately 70% of the exit speed at x/D = 12. Once again, this was a much more gradual decrease than seen at low Stokes number in Figure 5b. Clearly, the effect of the mass loading was small, with variation on the order of the measurement uncertainty.

We also examined the behavior of the centerline velocities for the rest of the conditions seen in Table 1. The behavior was consistent, showing a clear dependence on the Stokes number and a negligible influence from the mass loading. A modest Reynolds number dependence was seen, but this cannot be separated from the Stokes number changes. Because of the clear influence of Stokes number seen in Figure 5b, we attribute most of the variation to that parameter. Regardless, the primary factor was particle inertia in each case.

Next, we considered the axial variation of the jet half-width, b_w, at different Stokes numbers. Here, the half-width is defined as the radial position when the axial velocity is one-half of the local centerline velocity. For a
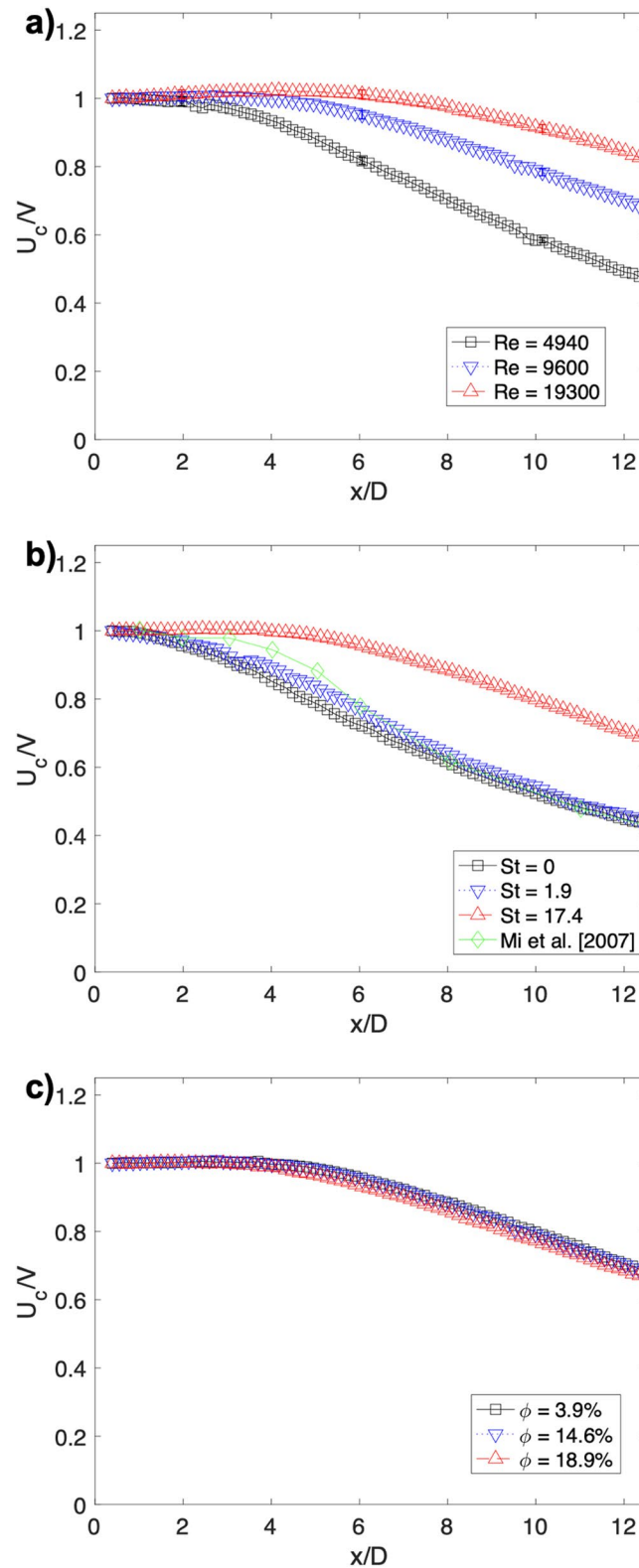
Figure 5. Ensemble-averaged axial velocities along the centerline for (a) Varying Reynolds number at $\Phi \sim 14\%$ (b) Varying Stokes number at $Re_D = 9{,}600$ and $\Phi \sim 3\%$ (c) Varying mass loading at $Re_D = 9{,}600$ and $St = 17.4$. Velocity is normalized by the exit speed, while axial position is normalized by the jet diameter. Error bars indicate the uncertainty at various axial positions. Also shown are digitized data from Mi et al. (2007) for a single-phase air jet at $Re_D = 72{,}000$.
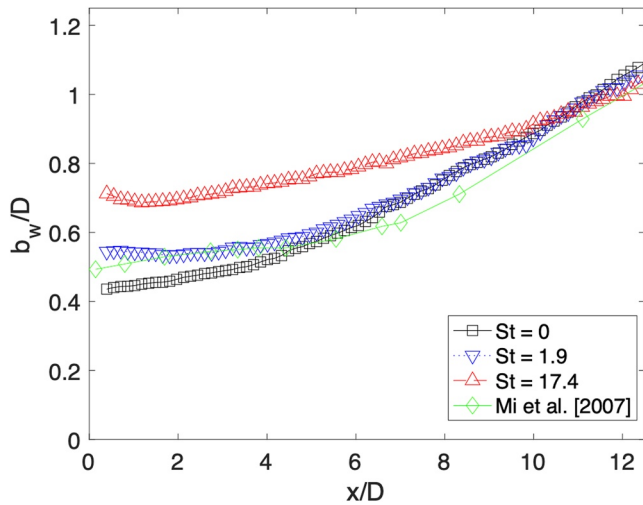
Figure 6. Ensemble-averaged half-widths for varying Stokes number at a Reynolds number of 9,600. The particle-laden cases had a mass loading of ~3%. Properties are normalized by the jet diameter. Also shown are digitized data from Mi et al. (2007) for a single-phase air jet at $Re_D = 72,000$.

self-similar, fully turbulent, single-phase jet, this parameter typically grows linearly with axial position, with a slope related to the entrainment from the ambient (Pope, 2000). In our two-phase jet, we examined the particle velocities, which may differ from the local velocity of the carrier fluid and the corresponding half-width. Even so, this parameter helps display how the flow develops downstream. Figure 6 shows the half-width development at $Re_D = 9,600$ and $\Phi \sim 3\%$, again comparing the nickel and hollow glass particles. Here, all properties are normalized by the jet diameter. In addition, the baseline, unladen case at this Reynolds number is also displayed.

Once again, the behavior was distinctly different as the Stokes number changes. For the hollow glass particles at lower St, the half-width changed gradually until around x/D ~ 6, maintaining a value slightly larger than the exit radius. After this short development length, the half-width grew approximately linearly until the end of the imaged region. This behavior was comparable to the unladen case with air alone, which also showed a short development length and a linear growth beyond. This response agreed well with previous single-phase experiments at a higher Reynolds number (Mi et al., 2007). With the hollow glass present, the half-width was larger near the exit than with air alone, but the sizes matched within the uncertainty by x/D ~ 6. This suggests that the entrainment behavior will be similar, but the magnitude will be reduced when particles are present. With the nickel-laden jet, the half-width was much larger near the exit, at approximately 70% of the diameter. The jet began to grow wider for x/D > 2, though the slope was smaller than either of the other cases. By x/D = 12, all three jets had nearly the same half-width. Because of the reduced slope, we expect that the entrainment would be moderated at high Stokes number. Note that the half-width response was similar at other Reynolds numbers.

We further examine the flow development using axial velocity profiles, as shown in Figure 7. These display the ensemble-averaged velocities normalized by the local centerline speed at successive streamwise positions. The radial position is normalized by the local half-width. Three flow conditions are considered, comparing the unladen air, hollow glass particle-laden, and nickel particle-laden jets at a Reynolds number of 9,600. The two particle-laden cases have a mass loading of ~3%.

At first glance, all three jets showed similar behavior. The flow exited the pipe with a log-law velocity profile (Saffaraval & Solovitz, 2012), which had a "fuller" shape with higher speeds near the half-width location. Farther downstream, the jets spread out, obtaining the expected Gaussian shape (Pope, 2000). Upon closer examination, there were slight differences, particularly when considering the higher-inertia nickel particles. Both air and hollow glass-laden jets reached a fully developed, Gaussian profile by x/D = 5, which agreed with previous measurements for single-phase jets (Mi et al., 2007; Saffaraval & Solovitz, 2012). At this modest Stokes number, the particle inertia does not significantly modify the mean velocity development. The nickel-laden jet had a fuller velocity profile near the exit than either of its counterparts, and it did not approach the Gaussian profile until farther downstream at x/D = 9. This again demonstrates that the inertia delays development, as seen in the centerline velocities and half-widths. This deviation is displayed clearly in Figure 8, which subtracts the unladen velocity profiles in Figure 7a from the particle-laden profiles in Figures 7b and 7c. As seen in Figure 8a, the hollow glass-laden jet was similar to the unladen air, deviating by less than 5% of the centerline speed after x/D = 3. From Figure 8b, the nickel-laden jet had higher speeds than the air at radial positions less than one half-width, with deviations of more than 10% of the centerline speed. Farther out radially, the nickel-laden jet had slower speeds, also deviating by more than 10%. These differences persisted until x/D = 9. Still, it is remarkable that the nickel-laden profile became Gaussian, even when the jet clearly was changing more slowly in Figures 5 and 6. This is a reminder that the fully developed mean velocity profile should not be construed as an indicator of self-similar conditions. We will see this more clearly when examining the turbulent fluctuations later.

3.3. Entrainment

The centerline data provided an indirect measure of entrainment, as seen in the slower development for higher-Stokes number jets. More directly, we used PIV measurements acquired using longer time delays, which
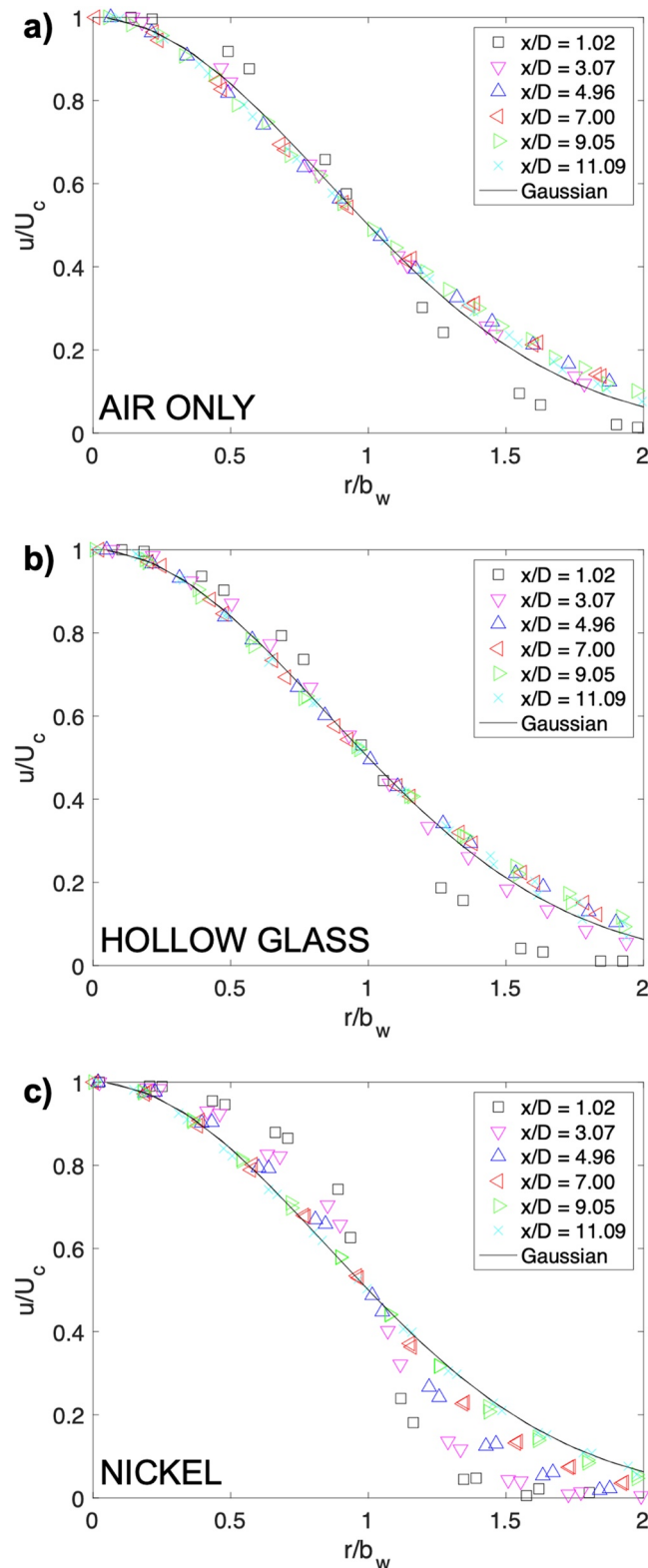
Figure 7. Ensemble-averaged axial velocity profiles at various streamwise positions for (a) Air alone (b) Hollow glass particles (St = 1.9) and (c) Nickel particles (St = 17.4). In all cases, the Reynolds number was fixed at 9,600. The particle-laden jet mass loading was ~3%. Axial velocity is normalized by the centerline speed at that streamwise position, while the radial position is normalized by the local half-width. A Gaussian profile is shown for comparison.
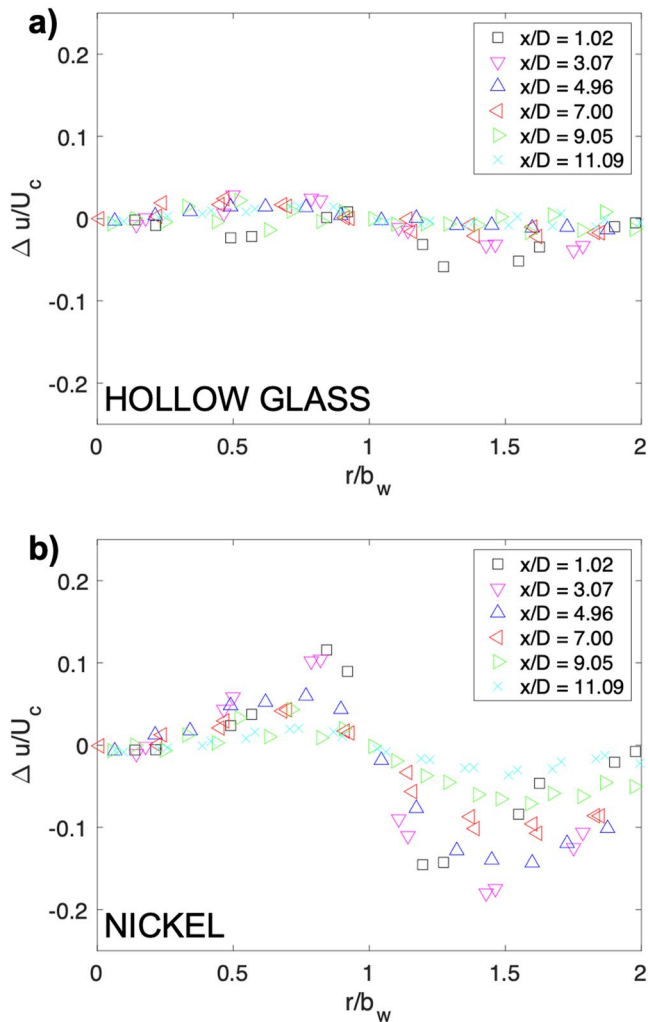
Figure 8. Deviation in ensemble-averaged axial velocity profiles compared to unladen air at various streamwise positions for (a) Hollow glass particles (St = 1.9) and (b) Nickel particles (St = 17.4). In all cases, the Reynolds number was fixed at 9,600. The particle-laden jet mass loading was ~3%. Axial velocity is normalized by the centerline speed at that streamwise position, while the radial position is normalized by the local half-width.

permitted higher-resolution study of the ambient flow around the jet. The ambient was seeded with aqueous glycol droplets, and we measured the velocities of the entrained air. For each test case, we ensemble-averaged all 1,000 instantaneous vector fields, which displayed the mean response away from the jet. Then, we examined the magnitude of the radial inflow velocity, v_r, as a function of radial position, r. From mass conservation at successive axial positions (Falcone & Cataldo, 2003), the axial gradient of the jet mass flow rate depends on this inflow velocity:

$$\frac{d \dot{m}}{dx} = 2\pi \rho_a r v_r \tag{1}$$

Here, ρ_a is the ambient air density. At larger radii, the quantity rv_r will approach a constant, which is used to determine the increase in mass flow. Typically, this is characterized by the entrainment ratio, calculated as:

$$\alpha = \frac{lim_{r \to \infty}(rv_r)}{b_w U_c} \tag{2}$$

This parameter normalizes the radial inflow using the local jet half-width and centerline velocity. Effectively, the entrainment ratio scales the inflow speed at the half-width to the centerline speed. Practically, the radial velocity can actually be outward at the half-width distance (Agrawal & Prasad, 2003), but the scaling is still commonly used in analysis of plume development. We only included radii more than two half-widths from the jet centerline, where rv_r was inward and approximately constant. We observed the same magnitude on both sides of the jet, as expected for axisymmetric conditions. Note that the half-width itself could be used to estimate the entrainment in fully developed flow, as the axial growth rate, db_w/dx, approaches a constant (Fischer et al., 1979; Pope, 2000). For these experiments, the flow is still developing, so such an estimate is not as accurate.
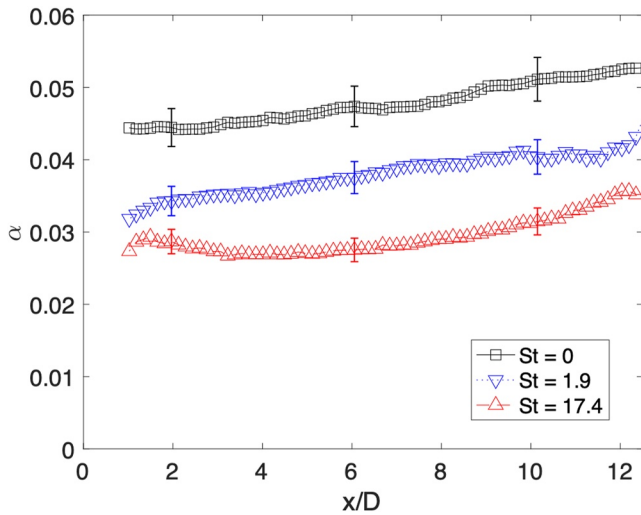
Figure 9 shows the entrainment ratio as a function of axial position for the same three cases compared in Figures 5b, 6, and 7. The unladen air jet showed a gradual increase in entrainment ratio over the first few diameters, rising from $\alpha \approx 0.045$ to 0.055 over 12 exit diameters. This modest axial dependence is expected in the near-exit region (Liepmann & Gharib, 1992; Ricou & Spalding, 1961; Solovitz & Mastin, 2009), and it has some impact on jet development, as discussed later. By the end of the test window, the entrainment ratio agreed with the expected level for a self-similar jet (Agrawal & Prasad, 2003; Fischer et al., 1979).

For the particle-laden jets, the entrainment ratio was lower at all axial positions, with more significant effects seen at higher Stokes number. For the low-St hollow glass particles, α was reduced by approximately 0.010 over the full test range, and it was nearly 20% less at x/D = 12. The entrainment ratio rose at approximately the same slope as the unladen case, though. The inertial effects were more pronounced for the nickel-laden jet. While the entrainment ratio was only slightly below the hollow glass-laden case near the exit, there was little growth over the test region at high St. This reduced slope corresponds with the earlier, indirect observations of entrainment in Figure 6, which showed slower development with increasing inertia. At x/D = 6, the entrainment ratio was 42% less than the unladen, single-phase air jet, which was a marked reduction. Even by the end of the test window, α only reached 0.035, which was still more than 30% lower.
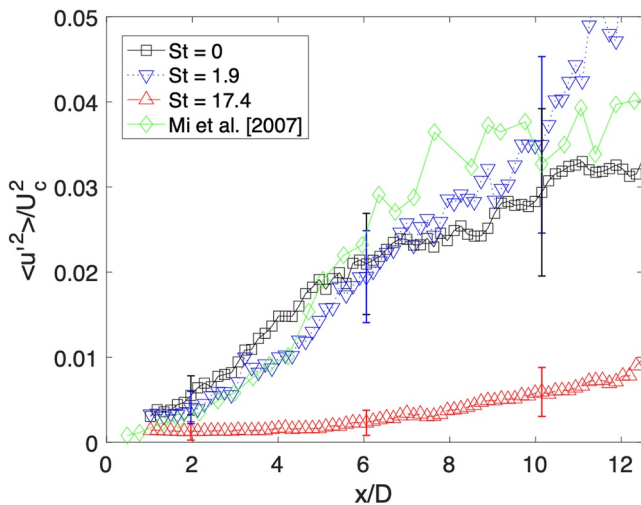
3.4. Turbulence Statistics

We next examined the turbulence of the flow using the statistics of the fluctuations about the mean field. For each test case, we subtracted the ensemble-averaged mean field from the instantaneous velocity fields, and then we averaged the correlations of these fluctuations about the mean. In this 2-D slice through the centerline, these resulted in the

Figure 9. Ensemble-averaged entrainment ratios for varying Stokes number. The Reynolds number was fixed at 9,600. The particle-laden jet mass loading was ~3%. Axial position is normalized by the jet diameter. Error bars indicate the uncertainty at various axial positions.

velocity variance in the axial and radial directions, $\langle u'^2 \rangle$ and $\langle v_r'^2 \rangle$, and a cross correlation, $\langle u'v_r' \rangle$. For the single-phase jet, these represent the Reynolds normal and shear stresses. For the particle-laden jets, where we measure particle velocities, these parameters consider the variance of the particle phase. Hence, these should not be construed as the carrier-phase turbulence statistics.

First, we considered the behavior along the centerline. Figure 10 shows the axial velocity variance as a function of streamwise position for different Stokes numbers. The variance is normalized by the local centerline velocity squared. The test conditions correspond to the same overlapping Reynolds numbers and mass loadings studied previously. The axial development was comparable to the mean flow behavior, with similar growth for the unladen and low-Stokes number particle-laden jets. By $x/D = 10$, the magnitude reached $\langle u'^2 \rangle/U_c^2 \approx 0.035$, which was on the same order seen for fully developed jets (Hussein et al., 1994). Past this point, the hollow-glass laden jet showed slightly higher fluctuations, though this was somewhat skewed due to higher uncertainty in this region. This higher uncertainty occurred because these positions are near the top of the laser sheet, where fewer particles were illuminated. As seen in Figure 2, the laser sheet displays particles up to $x/D \sim 14$, after which few particles are visible. In addition, the jet half-width grows downstream, reducing the particle density within each interrogation region after $x/D \sim 10$. Each of these factors affects the uncertainty of the instantaneous fluctuations, as displayed with the error bars in Figure 10. At higher Stokes number, the nickel-laden jet showed very little change over the test

region, maintaining a low fluctuation level throughout. The variance was significantly below the other cases, differing by a factor of 10 at $x/D = 6$. Clearly, the turbulent fluctuations of the particles were subdued with the high-inertia nickel. This reduction in turbulence fits with the finding of reduced entrainment in Figure 9, as that inflow was driven by turbulent eddies within the shear layer. Because the turbulent variation was reduced for the dispersed particles, the entrainment should correspondingly decrease. To be fair, reduced particle fluctuations do not necessarily imply that turbulence is modulated in the air carrier phase. Still, attenuation is typically observed for the scales considered here (Balachandar & Eaton, 2010). Although not shown here, the same behavior was seen with the radial velocity variance, as the fluctuations were greatly reduced at high St.
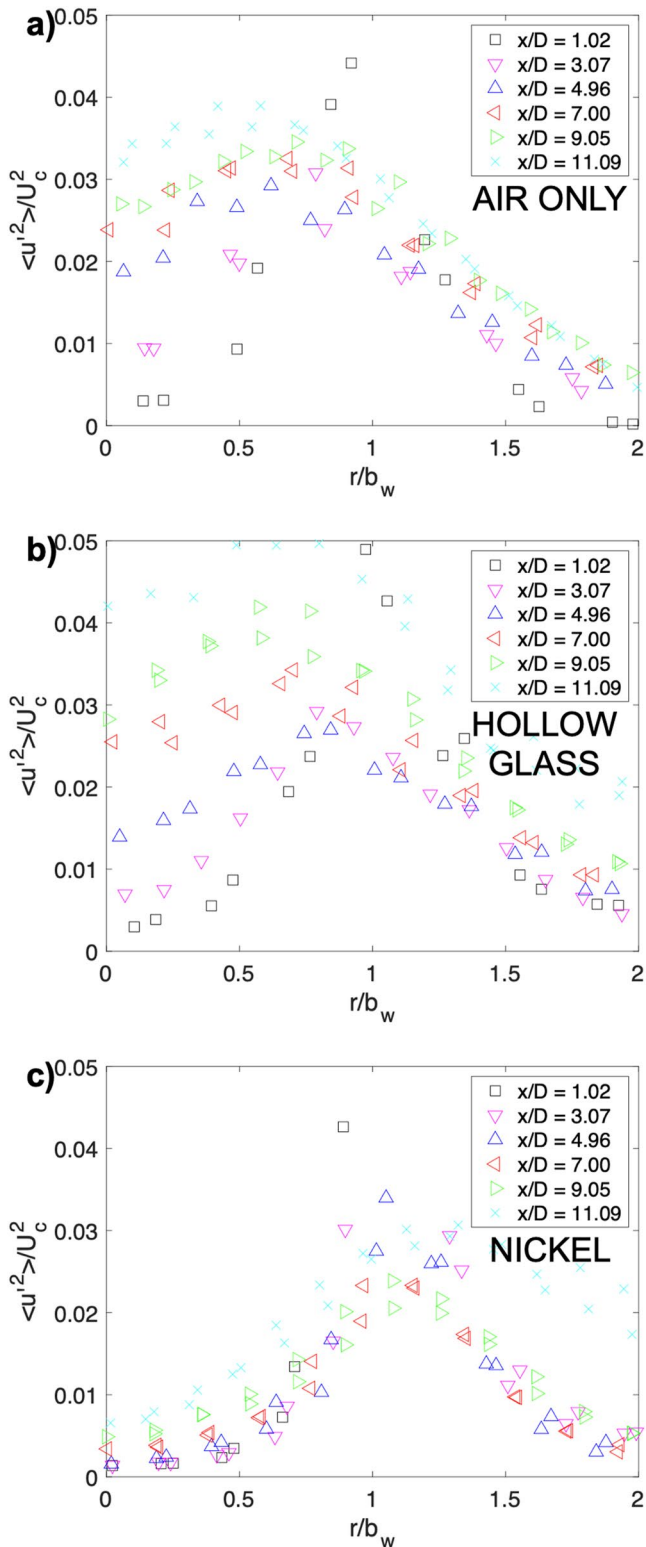

Figure 10. Ensemble-averaged axial velocity variance along the centerline for varying Stokes number. In all cases, the Reynolds number was fixed at 9,600. The particle-laden jet mass loading was ~3%. The variance is normalized by the local centerline speed squared, while axial position is normalized by the jet diameter. Error bars indicate the uncertainty at various axial positions. Also shown are digitized data from Mi et al. (2007) for a single-phase air jet at $Re_D = 72,000$.

Even more pronounced were the differences seen in the transverse profiles, which are illustrated in Figure 11. Here, we compare the axial velocity variance for different streamwise positions, considering the unladen jet and the two particle-laden jets at similar mass loading and Reynolds number. Statistics are normalized similar to Figure 10. Because the particles were concentrated within the shear layer and the jet core, the profiles only extend out to twice the half-width. At greater radial positions, the accuracy of the PIV measurements was significantly reduced due to the lack of particles. For unladen and hollow glass-laden air, shown in Figures 11a and 11b, respectively, there was gradual development of the variance throughout the test region. Near the jet exit, the profile was concentrated in a peak near the half-width location, with near-zero fluctuation within the jet core. Traveling downstream, the peak diffused outward, eventually spreading throughout the core. These trends agree with previous near-exit studies of turbulence (Mi et al., 2007; Saffaraval & Solovitz, 2012). By x/D of 10, the variance was at $\langle u'^2 \rangle/U_c^2 \approx 0.035$ throughout the jet, falling off outside the shear layer. These magnitudes were approaching, though still below, the fully developed conditions seen for single-phase jets much farther downstream (Hussein et al., 1994). Most critically, the low-St particle-laden jet showed very similar growth to the unladen case at all streamwise positions.

The nickel-laden air jet, seen in Figure 11c, showed virtually no development throughout the entire test region. Near the exit, there was still a peak at the half-width, indicative of the significant velocity difference across the shear

Figure 11. Ensemble-averaged axial velocity variance profiles at various streamwise positions for (a) Air alone (b) Hollow glass particles (St = 1.9) and (c) Nickel particles (St = 17.4). In all cases, the Reynolds number was fixed at 9,600. The particle-laden jet mass loading was ~3%. The variance is normalized by the centerline speed squared at that streamwise position, while the radial position is normalized by the local half-width.

layer itself. Within the jet, the fluctuations were small, with magnitudes similar to the other two jets in Figures 11a and 11b. Downstream, though, the high-St case maintained the same level of fluctuations over the entire test region, remaining at $\langle u'^2 \rangle / U_c^2 \approx 0.005$ by $x/D \approx 10$. This distinct difference could be seen throughout the jet core, as displayed in Figure 12, which presents the profiles for all three Stokes numbers at $x/D = 7.0$. Because of the high particle inertia, the turbulent fluctuations of the particles were essentially negligible compared to a single-phase jet. When considering the other correlation components, $\langle v_r'^2 \rangle$ and $\langle u'v_r' \rangle$, the same pattern was observed, although the magnitudes were smaller than the axial variance. At low Stokes number, the particle fluctuations grew similar to the unladen air jet. At high Stokes number, the fluctuations remained nearly negligible throughout the test region. For the other Reynolds numbers and mass loadings listed in Table 1, this response was observed in each test case. Clearly, the dominant factor was the Stokes number. Although not shown here, we also observe similar behavior with the turbulent kinetic energy spectra. Single-phase air and hollow-glass laden air had similar energy densities within the jet core, which followed the expected −5/3 power law (Pope, 2000). The nickel-laden air jet had significantly lower energy density within the jet core.

4. Discussion

4.1. Experimental Scaling and Relevance to Volcanic Plumes

To understand the implications and limitations of these experiments, we consider how these Reynolds numbers, Stokes numbers, and mass loadings compare to explosive eruptions in nature. Volcanic plumes start out as particle-laden jets exiting at velocities of tens to hundreds of meters per second, from vents with diameters of meters to hundreds of meters (Woods, 1995). Particles range in diameter from microns to meters, with densities ranging from >2,500 to about 500 kg/m³ for vesicular pumice or scoria clasts. When exiting the vent, volcanic jets tend to have solid mass fractions of 95%–99%, temperatures of 800°–1150°C, and mixture densities of several kilograms per cubic meter, which is several times that of air (Mastin, 2007). Negative buoyancy and entrainment of ambient air cause the plume's average ascent velocity to decrease with altitude, and the plume diameter to enlarge. If the plume entrains and heats enough ambient air to become buoyant, then it may accelerate again, reaching many kilometers in altitude.

The ascent of a volcanic plume can be calculated numerically by dividing the plume into a series of control volume steps and calculating changes in mass, momentum, and energy flux at each step. Figure 13 illustrates the evolution of two example plumes of different sizes, calculated using this control volume method with the 1-D model Plumeria (Mastin, 2014). Additional details of this model are provided in Appendix A. Figure 13a through 13e display the average ascent velocity, mixture density, plume radius, mass fraction of solids, and Reynolds number, respectively.

The properties in Figure 13a through 13c may be used to determine the Reynolds and Stokes numbers directly. If we assume that the viscosity of the plume mixture is roughly that of air at the same temperature (2.5×10^{-5} Pa-s), then the Reynolds numbers are 4×10^5 to 8×10^6, as shown in Figure 13e. This is much higher than the values (5,000–20,000) in the analogue experiments, as expected, though all cases are fully turbulent. In addition, the
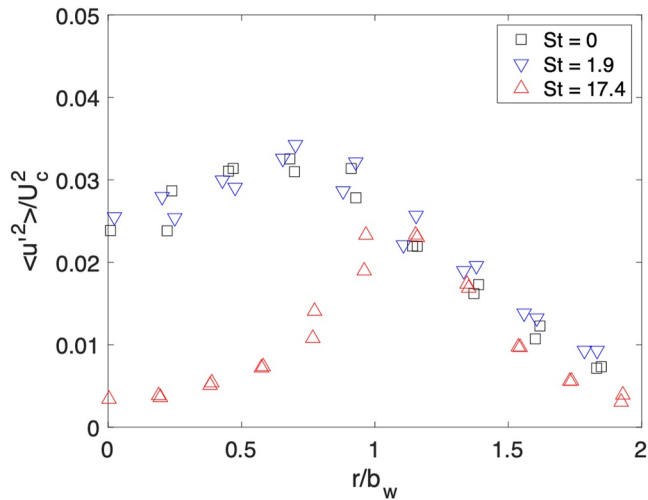
Figure 12. Ensemble-averaged axial velocity variance profiles at various Stokes numbers at $x/D = 7.0$. In all cases, the Reynolds number was fixed at 9,600. The particle-laden jet mass loading was $\sim$3%. The variance is normalized by the centerline speed squared at that streamwise position, while the radial position is normalized by the local half-width.

experimental Stokes number range would require relatively large particle diameters in volcanic plumes, from about 2.5 to 11.3 mm for the small plume and 2.9 to 13.0 mm for the large plume. From Figure 13d, it is apparent that mass loadings of 5%–10%, used in these experiments, occur at a few to several kilometers above the vent in natural settings. As seen in Figure 13, the modeled plumes eventually rise more than 10 km above their vents. The modeled plume at Mount Spurr rises to approximately 12.6 km above the vent, while the modeled plume at Mount St. Helens reaches approximately 17.2 km above the vent.

Table 2 provides the particle sizes that correspond to the experimental Stokes numbers from $\sim$1 to $\sim$20. At the vent, assuming a particle density of approximately 1,000 kg/m^3, the relevant particle diameters are about 0.8–3.6 mm for the small plume and 1.3–5.8 mm for the larger one. At higher elevations above the vent, particle mass loadings are comparable to these experiments. These occur at approximately 4 km for the small plume and 8 km for the large plume. In silicic eruptions, most particle diameters tend to be much smaller than 1 mm. For the Mount St. Helens eruption, extensive deposit sampling and analysis found that more than 95% of particles were smaller than 1 mm in diameter (Durant et al., 2009). For the 18 August 1992 Mount Spurr eruption, the percentage is about 80% (Durant & Rose, 2009). Thus, most of the erupted particles are too small to alter the large-scale turbulence of the flow, or the entrainment rates, although the largest particles have been shown to affect entrainment in Figure 9. More coarse-grained eruptions may show more significant variation.

4.2. Implications of Reduced Entrainment

For volcanic eruptions, reduced entrainment may have a significant impact on the likelihood of volcanic column collapse. Without sufficient entrainment, the plume may not become positively buoyant, which can result in column collapse when mass eruption rates are higher than a critical level. The entrained mass flow scales with the circumference of the plume, which increases linearly with its diameter. However, the mass eruption rate scales with the cross-sectional area, increasing with the diameter squared. Hence, the ratio between the entrained mass flow and the mass eruption rate is inversely proportional to the plume diameter. Now, if the entrainment ratio is modified by a certain scaling factor, then the plume diameter must be adjusted by the same factor to maintain the same ratio between the erupted and entrained mass flows. Because the eruption rate scales quadratically with diameter, the adjusted eruption rate will then change by the scaling factor squared. Averaging over the test region ($0 < x/D < 12$) in Figure 9, the nickel-laden jet had an entrainment ratio that was 39% less than single-phase air, with a maximum reduction of 42% at $x/D = 6$. By the quadratic scaling, a 39% average reduction in entrainment ratio corresponds to a 63% reduction in the critical mass eruption rate, while the 42% maximum reduction in entrainment corresponds to a 66% decrease in critical mass eruption rate. Using either metric, the overall decrease is nearly threefold. This approximate scaling analysis has been confirmed using 1-D plume models (Mastin, 2007; Saffaraval et al., 2012), such as Plumeria. As seen in Figure 9, the deviation in entrainment ratio extended beyond our test region to $x/D > 12$. Thus, the effect on critical mass eruption rate may be larger than estimated here, though we do not want to extrapolate without more data. Although not shown here, we also examined the entrainment ratio for the three different mass loadings of nickel particles shown in Figure 5c. Each of the cases showed little change in entrainment ratio over the test region, and all displayed levels below the unladen and hollow-glass laden jets. Higher mass loadings had slightly lower values of α, though the reduction was comparable to the experimental uncertainty.

Initially, the decrease in entrainment seems counter to some previous studies for particle-laden plumes. Using a 3-D large eddy simulation, Cerminara et al. (2016) found a modest increase in the entrainment ratio in the buoyant region, with values between 0.1 and 0.25 for different eruptions. These simulations included a kinematic decoupling model for the particles, though the Stokes numbers were relatively low (<0.2) in each case. Lherm and Jellinek (2019) conducted entrainment experiments with a canonical flow, studying grid-stirred turbulence in
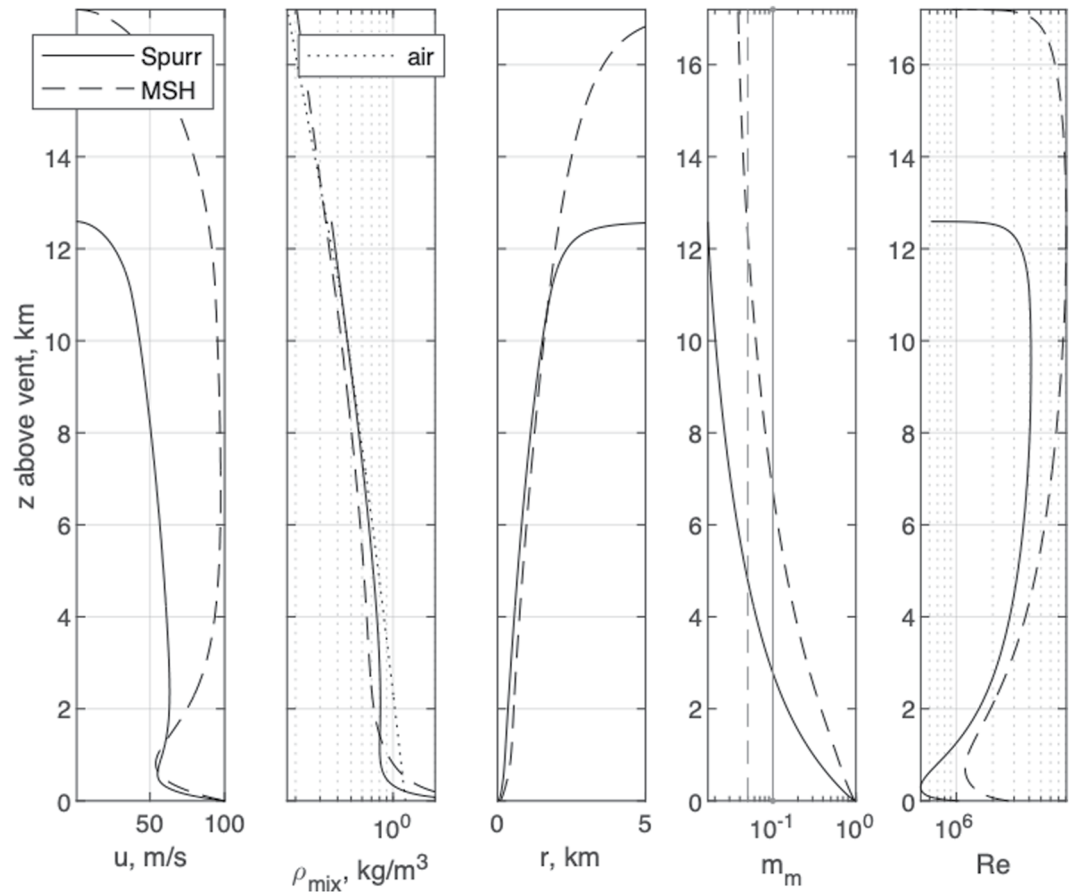
Figure 13. Comparison of experimental and natural volcanic plume parameters using the one-dimensional model Plumeria (Mastin, 2014). This shows modeled evolution of (a) plume ascent velocity (b) mixture density (c) plume radius (d) mass fraction of solids and (e) Reynolds number. Results are shown for two volcanic plumes. The solid black line represents a mass eruption rate (3×10^6 kg/s) similar to the 18 August 1992 Mount Spurr eruption in Alaska (McGimsey et al., 2001). The dashed black line represents an eruption rate (2×10^7 kg/s) similar to the 18 May 1980 Mount St. Helens eruption in Washington (Carey & Sigurdsson, 1982). The dashed and solid gray lines in (d) bound the range of 5%–10% mass loading used in these experiments. Additional details are provided in Appendix A.

a density-stratified water tank. By examining the growth of the density interface between fluid layers, they esti-mated that large particles enhanced entrainment by 37%. Smaller particles slightly reduced entrainment, though. These tests also considered modestly low Stokes numbers, on the order of one or less. Most recently, Gilchrist and Jellinek (2021) examined particle-laden jets in a stratified water tank, examining their growth up to the umbrella

Table 2
Particle Sizes That Correspond to Stokes Numbers Used in the Experiments, Assuming Plume Behavior From Two Well-Characterized Eruptions at Mount Spurr and Mount St. Helens

Eruption	Elevation (km)	Plume diameter (km)	Plume velocity (m/s)	Temperature (K)	Viscosity (Pa-s)	Particle diameter (mm) at St = 1	Particle diameter (mm) at St = 20
Spurr	0	0.08	100	1173	4.63×10^{-5}	0.82	3.65
MSH	0	0.205	100	1173	4.63×10^{-5}	1.31	5.85
Spurr	4	1.134	61.1	314	1.92×10^{-5}	2.53	11.32
MSH	8	2.499	97	296	1.83×10^{-5}	2.92	13.04

Note. Plume diameter, velocity, and temperature were calculated in the 1-D plume model runs illustrated in Figure 13. Viscosity is calculated from plume temperature using a relationship described in Appendix A. The diameters of particles at a given Stokes number were calculated from the parameter definition given in Section 2.4, assuming a particle density of 1,000 kg/m³.

cloud. By fitting the response to a 1-D plume model, they estimated the entrainment ratio, which exceeded 0.1 under some buoyancy conditions. Stokes numbers were larger in these experiments, reaching nearly six in some tests.

However, there are clear reasons why our experiments showed different entrainment behavior. First, we considered Stokes numbers that were higher, with values ranging from ∼1 to >20. Second, we did not examine buoyant conditions, which have higher entrainment even for single-phase fluids (Mastin, 2007). Our experiments focused on the region immediately above the jet exit, where gas and particles are both undergoing a rapid deceleration. In the buoyant region, the flow may accelerate, particularly as the plume becomes positively buoyant. Third, and most importantly, we examined particle sizes where turbulence typically would be attenuated. When particle diameters are smaller than one-tenth of the integral length scale, there is usually a reduction in turbulence (Balachandar & Eaton, 2010). For a jet, the integral length scale is on the same order as the jet diameter (Pope, 2000), and our particles were far smaller than this level. Reduced turbulence corresponds to decreased mixing and entrainment in the flow.

One related study did suggest that entrainment would decrease in the presence of high-inertia particles. Jessop and Jellinek (2014) examined the behavior of buoyant plumes in a stratified water tank, varying the particle Stokes number and the vent exit profile. By measuring the half-width variation, they estimated the entrainment ratio. When the vent geometry was flared outward, the entrainment again increased for high-Stokes number particles. Greater entrainment instead increases the critical mass eruption rate for column collapse, as demonstrated with 1-D plume models (Mastin, 2007). However, when the vent geometry was vertical, entrainment was approximately 40% lower. This reduction was attributed to stretching of the large-scale vortices by the high-inertia particles. This reduced their radial penetration distance and the associated mixing. Vent shape can also have significant effects on flow structure (McNeal et al., 2018; Ogden, 2011) and turbulence development (Mi et al., 2001). While our experiments focused on a cylindrical exit only, it is reasonable that the shape played some role in the entrainment behavior. As seen in Figures 7 and 8, higher-inertia particles produced fuller velocity profiles, which could distort the eddies near the exit.

4.3. Turbulence Modulation

At higher Stokes numbers, we measured significantly lower fluctuations in the particle phase. Although this does not necessarily coincide with reduced turbulence in the carrier fluid, the particle and fluid scales should correspond to attenuation (Balachandar & Eaton, 2010). Our test conditions fall within the two-way coupled regime, as we have low volumetric loadings with more modest mass loadings. In this regime, the carrier and dispersed phases should influence each other, even if there is limited direct particle interaction. Several mechanisms have been identified for turbulence modulation, such as increased mixture inertia and viscosity due to the mass loading. For the lowest loadings, these effects should be modest. The most important driver may be enhanced dissipation from the particles. Because of their greater inertia, they do not respond rapidly to fluid fluctuations. The corresponding particle forces produce energy transfer to the nearby fluid region, where scales are small enough to promote rapid dissipation. High-resolution studies have demonstrated that particles distort the surrounding turbulent eddies (Tanaka & Eaton, 2010), but these experiments have primarily focused on homogeneous and isotropic conditions. The behavior may be similar within jets, but more information is needed about this process.

5. Conclusions

We experimentally studied the behavior of particle-laden flows over a range of Reynolds numbers, Stokes numbers, and mass loadings relevant to volcanic eruption plumes. The Reynolds numbers considered a range of turbulent conditions, while the Stokes numbers corresponded to both high and low inertia cases. At the highest Stokes numbers, the particle inertia dominated any particle turbulence fluctuations. At the lowest levels, the particle turbulent behavior was similar to the single-phase, particle-free gas. The mass loadings ranged from nearly negligible levels of 0.3% to nearly 20% particles, which compares to real volcanic plumes at heights of 4–8 km above the vent in two modeled examples of large, sustained eruptions. Of the three parameters considered, the Stokes number had the most significant effect on the velocity and particle turbulence statistics, while the Reynolds number and mass loading had secondary impact.

Particle inertia had a marked influence on the entrainment of ambient air into the jet. At low Stokes number, the entrainment ratio was modestly reduced compared to the unladen air jet, though its slope was similar. At a

high Stokes number of 17.4, the entrainment ratio remained roughly constant over the same region. By six vent diameters downstream, the entrainment ratio was reduced by 40% compared to the particle-free cases. From a geophysical perspective, this reduced entrainment would increase the likelihood of column collapse for a cylindrical vent, as it corresponds to a threefold reduction in the maximum eruption rate for a buoyant plume. Since the flow was still developing by x/D of 12, the actual reduction may be even larger. The Stokes number also had a significant influence on the particle turbulence. At low Stokes numbers, nearer to one, the variance of axial velocity fluctuations had a magnitude and distribution similar to a particle-free air jet. At high Stokes numbers, near 20, the axial variance was substantially reduced, and it remained lower throughout the measurement region. As a result, particle motion would be greatly reduced within the plume, which explains the reduced entrainment measurement. For eruptions with larger, coarse grains, these results suggest that decreased turbulence and entrainment may make it easier for volcanic plumes to collapse.

Finally, these findings suggest several directions for future experiments. First, the turbulent behavior of both phases could be explored simultaneously rather than independently, using the same PIV images to examine different particles. Previous studies have usually required very dilute loadings, though other methods can discern the particles and oil droplets, such as image filtering by particle size, brightness, or region of interest. Special fluorescent coatings could mask some particles, though these can be expensive. Second, higher-resolution experiments would permit study of the smaller-scale behavior, notably near the Kolmogorov scale. This would also help distinguish the details of the turbulent kinetic energy (and perhaps enstrophy) spectra, which could be used to study the entrainment process within turbulent eddies. Third, the particle distribution could be examined within the jet flow, as preferential concentration can promote collisions and eventual aggregation. Fourth, other pertinent variables could be explored, such as vent shape and relative humidity. These should also have a direct influence on aggregation. Finally, there are additional impacts of reduced entrainment that could be explored, such as the partitioning of erupted mass between the ground and the atmosphere.

Appendix A: Plume Model Conditions

Inputs to the 1-D plume model presented in Figure 13 include magma temperature, gas content, vent diameter, ejection velocity, and a sounding of temperature, pressure and humidity in the atmosphere. These model runs each assumed a magma temperature of 900°C, magma gas content of 3 wt% (assumed to be H_2O), an exit velocity of 100 m/s, and atmospheric properties specified by the U.S. Standard Atmosphere (United States Committee on Extension to the Standard Atmosphere, 1976). The model used the specified magmatic temperature and gas content to calculate a mixture density at the vent, and then multiplied this density by the ascent velocity and the vent cross-sectional area to calculate mass eruption rate. We adjusted the vent diameter until the mass eruption rate agreed with eruption rates published for these eruptions. The resulting vent diameters were 80 and 205 m, respectively. The model assumed that the inward velocity of air entering the plume at its margins is 9% of the average upward velocity of the plume. The Reynolds number in Figure 13e was calculated by assuming that the mixture viscosity equals that of air at the same temperature, which was calculated using the formula:

$$\mu_{mix} = 0.0000172 \left(\frac{390}{T_{mix} + 117} \right) \left(\frac{T_{mix}}{273} \right)^{1.5} \tag{A1}$$

here, μ_{mix} is viscosity in Pa-s and T_{mix} is mixture temperature in K (Moran & Shapiro, 1992). Additional details are provided by Mastin (2007, 2014).

Nomenclature

b_w	jet half-width
D	jet exit diameter
D_p	mean particle diameter
f	correction factor to particle response time
g	gravitational acceleration
m_m	mass fraction of solids
$\dot{m}$	jet mass flow rate

$\dot{m}_f$	fluid mass flow rate
$\dot{m}_p$	particle mass flow rate
r	radial position; plume radius
Re_D	Reynolds number based on jet exit diameter, $\rho VD/\mu$
Re_p	particle Reynolds number
Ri	Richardson number, $\Delta\rho gD/(\rho V^2)$
St	Stokes number based on convective fluid timescale, $\rho_p D_p^2 V/(18\mu D)$
T_{mix}	mixture temperature
u	ensemble-averaged axial velocity; plume ascent velocity
U_c	ensemble-averaged axial centerline velocity
$\langle u'^2\rangle$	axial velocity variance
$\langle u'v_r'\rangle$	cross-correlation of axial and radial velocity fluctuations
V	jet exit speed
v_r	ensemble-averaged radial velocity
v_x	instantaneous axial velocity
v_z	instantaneous transverse velocity
$\langle v_r'^2\rangle$	radial velocity variance
x	axial position
z	transverse position; elevation

Greek letters

α	entrainment ratio
ε	dissipation rate
μ	viscosity of carrier fluid
μ_{mix}	mixture viscosity
ν	kinematic viscosity of carrier fluid
ρ	jet fluid density
ρ_a	ambient air density
ρ_{mix}	mixture density
ρ_p	particle density
Σ	sedimentation number
τ_k	Kolmogorov time scale
Φ	mass loading, $\dot{m}_p / \dot{m}_f$
ω	vorticity

Acronyms

CCD	charge-coupled device
LDA	laser Doppler anemometry
PDA	phase Doppler anemometry
PIV	particle image velocimetry

Data Availability Statement

All PIV vector fields and processed velocity data (Solovitz, 2022) are accessible at https://doi.org/10.7910/DVN/HDBMHV.

References

Agrawal, A., & Prasad, A. K. (2003). Integral solution for the mean flow profiles of turbulent jets, plumes, and wakes. *Journal of Fluids Engineering*, *125*(5), 813–822. https://doi.org/10.1115/1.1603303

Balachandar, S., & Eaton, J. K. (2010). Turbulent dispersed multiphase flow. *Annual Review of Fluid Mechanics*, *42*, 111–133. https://doi.org/10.1146/annurev.fluid.010908.165243

Banko, A. J. (2018). *"Radiation absorption by inertial particles in a turbulent square duct flow," PhD thesis*. Stanford University.

Bell, J. H., & Mehta, R. D. (1988). *Contraction design for small low-speed wind tunnels*. Technical Report JIAA-TR-84, NASA-CR-182747. Stanford University.

Briggs, G. A. (1965). A plume rise model compared with observations. *JAPCA*, *15*(9), 433–438. https://doi.org/10.1080/00022470.1965.10468404

Carazzo, G., & Jellinek, A. M. (2012). A new view of the dynamics, stability and longevity of volcanic clouds. *Earth and Planetary Science Letters*, *325*, 39–51. https://doi.org/10.1016/j.epsl.2012.01.025

Carey, S. N., & Sigurdsson, H. (1982). Influence of particle aggregation on deposition of distal tephra from the May 18, 1980, eruption of Mount St. Helens volcano. *Journal of Geophysical Research*, *87*(B8), 7061–7072. https://doi.org/10.1029/JB087iB08p07061

Cerminara, M., Ongaro, T. E., & Neri, A. (2016). Large eddy simulation of gas–particle kinematic decoupling and turbulent entrainment in volcanic plumes. *Journal of Volcanology and Geothermal Research*, *326*, 143–171. https://doi.org/10.1016/j.jvolgeores.2016.06.018

Coleman, S. W., & Vassilicos, J. C. (2009). A unified sweep-stick mechanism to explain particle clustering in two-and three-dimensional homogeneous, isotropic turbulence. *Physics of Fluids*, *21*(11), 113301. https://doi.org/10.1063/1.3257638

Costa, A., Suzuki, Y. J., Cerminara, M., Devenish, B. J., Ongaro, T. E., Herzog, M., et al. (2016). Results of the eruptive column model inter-comparison study. *Journal of Volcanology and Geothermal Research*, *326*, 2–25. https://doi.org/10.1016/j.jvolgeores.2016.01.017

Durant, A., & Rose, W. I. (2009). Sedimentological constraints on hydrometeor-enhanced particle deposition: 1992 eruptions of Crater Peak, Alaska. *Journal of Volcanology and Geothermal Research*, *186*(1–2), 40–59. https://doi.org/10.1016/j.jvolgeores.2009.02.004

Durant, A. J., Rose, W. I., Sarna-Wojcicki, A. M., Carey, S., & Volentik, A. C. (2009). Hydrometeor-enhanced tephra sedimentation: Constraints from the 18 May 1980 eruption of Mount St. Helens (USA). *Journal of Geophysical Research*, *114*(B3), B03204. https://doi.org/10.1029/2008JB005756

Eaton, J. K., & Fessler, J. R. (1994). Preferential concentration of particles by turbulence. *International Journal of Multiphase Flow*, *26*, 719–727. https://doi.org/10.1016/0301-9322(94)90072-8

Falcone, A. M., & Cataldo, J. C. (2003). Entrainment velocity in an axisymmetric turbulent jet. *Journal of Fluids Engineering*, *125*(4), 620–627. https://doi.org/10.1115/1.1595674

Fischer, H. B., List, E. J., Koh, R. C. Y., Imberger, J., & Brooks, N. H. (1979). *Mixing in inland and coastal waters*. Academic Press.

Gilchrist, J. T., & Jellinek, A. M. (2021). Sediment waves and the gravitational stability of volcanic jets. *Bulletin of Volcanology*, *83*(10), 1–59. https://doi.org/10.1007/s00445-021-01472-1

Han, D. (2001). *"Study of turbulent nonpremixed jet flames using simultaneous measurements of velocity and CH distribution," PhD thesis*. Stanford University.

Hoffman, D. W., Solovitz, S. A., Eaton, V. A. R., Mastin, L. G., & Eaton, J. K. (2020). Experimental study of particle aggregation in a humid and turbulent environment. In *Proceedings of the AGU fall meeting*. V016-0015.

Hussein, H. J., Capp, S. P., & George, W. K. (1994). Velocity measurements in a high-Reynolds-number, momentum-conserving, axisymmetric, turbulent jet. *Journal of Fluid Mechanics*, *258*, 31–75. https://doi.org/10.1017/s002211209400323x

Hwang, W., & Eaton, J. K. (2006). Homogeneous and isotropic turbulence modulation by small heavy (St ∼ 50) particles. *Journal of Fluid Mechanics*, *564*, 361–393. https://doi.org/10.1017/S0022112006001431

Jessop, D. E., & Jellinek, A. M. (2014). Effects of particle mixtures and nozzle geometry on entrainment into volcanic jets. *Geophysical Research Letters*, *41*(11), 3858–3863. https://doi.org/10.1002/2014GL060059

Kays, W. M., & Crawford, M. E. (1993). *Convective heat and mass transfer* (2nd ed.). McGraw-Hill.

Lau, T. C. W., & Nathan, G. J. (2014). "Influence of Stokes number on the velocity and concentration distributions in particle-laden jets. *Journal of Fluid Mechanics*, *757*, 432–457. https://doi.org/10.1017/jfm.2014.496

Lau, T. C. W., & Nathan, G. J. (2015). The influence of Stokes number on particle clustering within a two-phase turbulent jet. In *Proceedings of the 7th Australian conference on laser diagnostics in fluid mechanics and combustion*. Australia.

Lau, T. C. W., & Nathan, G. J. (2017). A method for identifying and characterising particle clusters in a two-phase turbulent jet. *International Journal of Multiphase Flow*, *88*, 191–204. https://doi.org/10.1016/j.ijmultiphaseflow.2016.10.002

Lherm, V., & Jellinek, A. M. (2019). Experimental constraints on the distinct effects of ash, lapilli, and larger pyroclasts on entrainment and mixing in volcanic plumes. *Bulletin of Volcanology*, *81*(12), 1–11. https://doi.org/10.1007/s00445-019-1329-2

Liepmann, D., & Gharib, M. (1992). The role of streamwise vorticity in the near-field entrainment of round jets. *Journal of Fluid Mechanics*, *245*, 643–668. https://doi.org/10.1017/s0022112092000612

Longmire, E. K., & Eaton, J. K. (1992). Structure of a particle-laden round jet. *Journal of Fluid Mechanics*, *236*, 217–257.

Mastin, L. G. (2007). A user-friendly one-dimensional model for wet volcanic plumes. *Geochemistry, Geophysics, Geosystems*, *8*(3). https://doi.org/10.1029/2006gc001455

Mastin, L. G. (2014). Testing the accuracy of a 1-D volcanic plume model in estimating mass eruption rate. *Journal of Geophysical Research: Atmospheres*, *119*(5), 2474–2495. https://doi.org/10.1002/2013JD020604

McGimsey, R. G., Neal, C. A., & Riley, C. (2001). *Areal distribution, thickness, volume, and grain size of tephra-fall deposits from the 1992 eruptions of Crater Peak vent, Mt Spurr volcano, Alaska*. U.S. Geological Survey Open-File Report 01-0370 (p. 38). U.S. Government Printing Office. https://doi.org/10.3133/ofr01370

McNeal, J. S., Jones, J., Cal, R. B., Mastin, L. G., Kim, D., & Solovitz, S. A. (2018). Experimental study of analogue vent erosion towards nozzle shapes. *Journal of Volcanology and Geothermal Research*, *367*, 79–87. https://doi.org/10.1016/j.jvolgeores.2018.10.022

Melling, A. (1997). Tracer particles and seeding for particle image velocimetry. *Measurement Science and Technology*, *8*(12), 1406–1416. https://doi.org/10.1088/0957-0233/8/12/005

Mi, J., Kalt, P., Nathan, G. J., & Wong, C. Y. (2007). PIV measurements of a turbulent jet issuing from round sharp-edged Plate. *Experiments in Fluids*, *42*(4), 625–637. https://doi.org/10.1007/s00348-007-0271-9

Mi, J., Nathan, G. J., & Nobes, D. S. (2001). Mixing characteristics of axisymmetric free jets from a contoured nozzle, an orifice plate and a pipe. *Journal of Fluids Engineering*, *123*(4), 878–883. https://doi.org/10.1115/1.1412460

Moran, M. J., & Shapiro, H. N. (1992). *Fundamentals of engineering thermodynamics* (p. 804). John Wiley and Sons, Inc.

Morton, B., Taylor, G., & Turner, J. (1956). Turbulent gravitational convection from maintained and instantaneous sources. *Proceedings of the Royal Society London Series A*, *234*, 1–23. https://doi.org/10.1098/rspa.1956.0011

Ogden, D. (2011). Fluid dynamics in explosive volcanic vents and craters. *Earth and Planetary Science Letters*, *312*(3–4), 401–410.

Pope, S. (2000). *Turbulent flows*. Cambridge University Press.

Prevost, F., Boree, J., Nuglisch, H. J., & Charnay, G. (1996). Measurements of fluid/particle correlated motion in the far field of an axisymmetric jet. *International Journal of Heat and Fluid Flow*, *22*(4), 685–701. https://doi.org/10.1016/0301-9322(96)00009-2

Pumir, A., & Wilkinson, M. (2016). Collisional aggregation due to turbulence. *Annual Review of Condensed Matter Physics*, *7*(1), 141–170. https://doi.org/10.1146/annurev-conmatphys-031115-011538

Raffel, M., Willert, C. E., & Kompenhans, J. (1998). *Particle image velocimetry: A practical guide*. Springer, Berlin.

Ricou, F. P., & Spalding, D. B. (1961). Measurements of entrainment by axisymmetrical turbulent jets. *Journal of Fluid Mechanics*, *11*, 21–32.

Saffaraval, F., & Solovitz, S. A. (2012). Near-exit flow physics of a moderately overpressured jet. *Physics of Fluids*, *24*(8). https://doi.org/10.1063/1.4745005

Saffaraval, F., Solovitz, S. A., Ogden, D. E., & Mastin, L. G. (2012). Impact of reduced near-field entrainment of overpressured volcanic jets on plume development. *Journal of Geophysical Research*, *117*(B5), B05209. https://doi.org/10.1029/2011jb008862

Sakakibara, J., Wicker, R. B., & Eaton, J. K. (1996). Measurements of the particle-fluid velocity correlation and the extra dissipation in a round jet. *International Journal of Multiphase Flow*, *22*(5), 863–881. https://doi.org/10.1016/0301-9322(96)00014-6

Solovitz, S. (2022). Particle-laden jet PIV data [Dataset]. Harvard Dataverse. https://doi.org/10.7910/DVN/HDBMHV

Solovitz, S. A., & Mastin, L. G. (2009). Experimental study of near-field air entrainment by subsonic volcanic jets. *Journal of Geophysical Research*, *114*(B10), B10203. https://doi.org/10.1029/2009JB006298

Solovitz, S. A., Mastin, L. G., & Saffaraval, F. (2011). Experimental study of near-field entrainment of moderately overpressured jets. *Journal of Fluids Engineering*, *133*(5). https://doi.org/10.1115/1.4004083

Sparks, R. S. J., Bursik, M. I., Carey, S. N., Gilbert, J. S., Glaze, L. S., Sigurdsson, H., & Woods, A. W. (1997). *Volcanic plumes*. Wiley.

Squires, K. D., & Eaton, J. K. (1990). Particle response and turbulence modulation in isotropic turbulence. *Physics of Fluids*, *2*, 1191–1203.

Stevenson, J. A., Millington, S. C., Beckett, F. M., Swindles, G. T., & Thordarson, T. (2015). Big grains go far: Understanding the discrepancy between tephrochronology and satellite infrared measurements of volcanic ash. *Atmospheric Measurement Techniques*, *8*(5), 2069–2091. https://doi.org/10.5194/amt-8-2069-2015

Sumbekova, S., Cartellier, A., Aliseda, A., & Bourgoin, M. (2017). Preferential concentration of inertial sub-Kolmogorov particles: The roles of mass loading of particles, Stokes numbers, and Reynolds numbers. *Physical Review Fluids*, *2*(2), 024302. https://doi.org/10.1103/physrevfluids.2.024302

Sundaram, S., & Collins, L. R. (1997). Collision statistics in an isotropic particle-laden turbulent suspension. Part 1. Direct numerical simulation. *Journal of Fluid Mechanics*, *335*, 75–109. https://doi.org/10.1017/s0022112096004454

Suzuki, Y. J., & Koyaguchi, T. (2015). Effects of wind on entrainment efficiency in volcanic plumes. *Journal of Geophysical Research*, *120*(9), 6122–6140. https://doi.org/10.1002/2015JB012208

Tanaka, T., & Eaton, J. K. (2010). Sub-Kolmogorov resolution particle image velocimetry measurements of particle-laden forced turbulence. *Journal of Fluid Mechanics*, *643*, 177–192.

United States Committee on Extension to the Standard Atmosphere. (1976). U.S. Standard atmosphere, National Oceanic and Atmospheric Administration (p. 227).

Wilson, T. M., Jenkins, S., & Stewart, C. (2015). In J. F. Shroder & P. Papale (Eds.), *Impacts from volcanic ash fall, volcanic hazards, risks and disasters* (pp. 47–86). Elsevier.

Woods, A. (1995). The dynamics of explosive volcanic eruptions. *Review of Geophysics*, *33*(4), 495–530. https://doi.org/10.1029/95RG02096